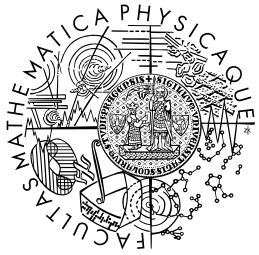

FACULTY
OF MATHEMATICS
AND PHYSICS
Charles University

DOCTORAL THESIS

Vít Gabriel

Kinetic Monte Carlo Simulations in Physics of Thin Films: from Growth to Electronic Properties

Department of Surface and Plasma Science

Supervisor of the doctoral thesis: doc. RNDr. Pavel Kocán, Ph.D.

Study programme: Physics of Plasmas and Ionized Media

Study branch: Physics of Plasmas and Ionized Media

Prague 2023

I declare that I carried out this doctoral thesis independently, and only with the cited sources, literature and other professional sources. It has not been used to obtain another or the same degree.

I understand that my work relates to the rights and obligations under the Act No. 121/2000 Sb., the Copyright Act, as amended, in particular the fact that the Charles University has the right to conclude a license agreement on the use of this work as a school work pursuant to Section 60 subsection 1 of the Copyright Act.

In ..... date ....

Author's signature

I would like to thank my partner and my family and everyone from P. Fík's team for their endless support.

I would like to thank my supervisor doc. RNDr. Pavel Kocán, Ph.D. for great support, guidance and patience during my whole doctoral studies. I am also grateful to prof. RNDr. Rudolf Hrach, DrSc. for leading me through my bachelor and master studies.

I would like to thank prof. RNDr. Václav Holý, CSc. for involving me in the PLD project and his leadership and many discussions. My thanks also belong to all the people who provided the experimental data – the pulsed-laser deposition group at Karlsruhe Institute of Technology. I would like to thank everyone in Martin Setvín's group at Charles University, especially doc. Mgr. Martin Setvín, Ph.D., and Jesús Redondo, Ph.D., and Dominik Wrana, Ph.D. who provided me with the data from the measurements of polarons.

This work was supported by projects GACR20-21727X and GAUK Primus/20/SCI/009.

Title: Kinetic Monte Carlo Simulations in Physics of Thin Films: from Growth to Electronic Properties

Author: Vít Gabriel

Department: Department of Surface and Plasma Science

Supervisor: doc. RNDr. Pavel Kocán, Ph.D., Department of Surface and Plasma Science

Abstract: Kinetic Monte Carlo (kMC) is a stochastic method used to simulate time evolution of a system. This algorithm finds application in various scientific fields. It is also widely used in physics of thin films. In the thesis, we developed models based on the kMC method to simulate growth and electronic properties of thin film.

First, we developed the model to simulate the pulsed-laser deposition (PLD) growth of multiferroic perovskite. The model was first validated with data from literature and then used to clarify some of the phenomena observed during PLD growth.

We innovatively explained the inter-layer transport crucial for film morphology using natural configuration-based processes. In addition, we were able to identify the cause of the experimentally observed decrease of surface roughness with increasing laser frequency.

Second, we used the kMC method to study polaron diffusion with the aim to further understand the charge transfer in doped hematite. We applied several approximations of how dopants could affect the charge transfer and found that they influence polaron diffusion globally rather than due to strong local effects. Moreover, our model suggests that the diffusion process depends on the polaron type. We also simulated the injection of hole polarons into doped hematite. Even using the general simulation setup, we were able to reproduce the measurements made during the injection process.

Keywords: Kinetic Monte Carlo, Pulsed-Lased Deposition, Polarons

Contents

Introduction

Monte Carlo (MC) methods are a family of algorithms which solve simulated problems using random numbers. They find application in variety of disciplines such as physics, especially in nuclear [Domain et al., 2004] and materials science [Ohno, 1999, Kroese et al., 2014], biology [Manly, 2021] or even economics [Brandimarte, 2014] and air traffic control [Lecchini Visintini et al., 2006]. The first MC algorithms were developed in 1940's and 1950's [Metropolis et al., 1953] in the form of Markov chain MC (MCMC) to simulate a stochastic process with probability density known up to a constant of proportionality. The probability density is represented by the Markov matrix that does not change during the simulation. The MCMC is used when it is not possible to find independent states of the stochastic process. Instead, the Markov chain of dependent states is formed [Geyer, 1992]. However, since the Markov matrix is constant, it is not possible to simulate the time evolution of the system. In order to study the time evolution, different methods must be used.

The most straightforward method to simulate development of the system in time is to solve the equations of motion for each particle of the system. This approach is the foundation of the molecular dynamics (MD) method [Alder and Wainwright, 1959]. The only necessary input to the simulation is the potential used in the equations of motion. The time evolution and the dynamic behavior of the system emerge naturally. The major disadvantage of the MD method for simulation of large systems is that many particles must be simulated and their positions and velocities calculated at each time step. The time-step must be sufficiently short to reduce the error of the numerical integration.

To overcome the simulation domain and time step limitations, the MC based algorithms are used to study the dynamical behavior of a larger system. For this purpose, the kinetic Monte Carlo (kMC) algorithm was developed [Bortz et al., 1975]. The kMC method was first used in 1966 to simulate radiation damage annealing Beeler [1966]. Since then, the method has been successfully used in a wide range of research areas including surface kinetics such as surface diffusion and growth [Andersen et al., 2019].

The kMC solves the global dynamic behavior of the system without the necessity to provide the exact evolution of each particle, although it is possible in principle [Voter, 2007]. Unlike in the MD, where the simulation domain is continuous, the usual implementation of the kMC method in physics of thin films is represented by lattice models [Andersen et al., 2019]. These models allow simulated units (atoms or molecules) to move only from and to predefined locations. The shortest time step is constrained by the time necessary to move from one lattice point to another. This process is usually limited by the diffusion barrier and thermally activated. Even though the exact microscopic behavior is not solved as precisely as in MD, it is possible to replicate measured macroscopic quantities with great accuracy Šmilauer and Vvedensky [1993]. This property of the kMC method is given by its stochastic nature. The capability to simulate larger system for long simulation times is not only an advantage but also a necessity.

In the thesis, we focus on two different applications of the kMC model in

physics of thin films. In Chapter 1, we give a brief introduction to the kMC method. In Chapters 2 and 3, we introduce two different implementations of the kMC model. In Chapter 2, we describe the simulation of the pulsed laser deposition (PLD) growth. The difficulty of this simulation lies in the opposing requirements. On the one hand, it is necessary to simulate each unit of the deposited material in order to achieve the highest possible accuracy. On the other hand, the growth temperature which influences the unit diffusion speed is very high. To overcome this problem, we designed a new implementation of the kMC method with infinitely fast diffusion. The results presented in this chapter are published in Gabriel et al. [2020, 2022a].

In Chapter 3, we introduce an effective implementation of the kMC based model for simulation of polarons diffusion. Polarons are quasiparticles which can form in polarizable materials by interaction of charge carrier (electron or hole) and lattice vibrations. Understanding their diffusion is of great importance for study and subsequent enhancment of charge transfer in such materials. The model is also used to simulate the interaction of polarons with dopants and defects inside hematite and the injection of polarons into the hematite. At the time of finishing this thesis the paper related to this topic is under review and can be downloaded from the repository Redondo et al. [2023].

1. Kinetic Monte Carlo

The Monte Carlo method is based on calculation of the system evolution by making random changes. The simplest example is the Markov chain Monte Carlo (MCMC) algorithm. In the MCMC algorithm, a new state is created by random perturbation of an original state. If the new state is more suitable, for example has lower energy than the previous one, it becomes the new original state. If it is not more suitable, a new perturbation on the original state is made. This process is repeated until the final state is reached.

To simulate the time evolution of the system, the kinetic Monte Carlo (kMC) was developed. There are two main types of the kMC algorithm, which differ in the choice of which new system configuration is accepted and how the list of possible processes is constructed:

- Rejection kMC - Every time-step a process is chosen randomly from the list of all the possible processes. The rate r_i is calculated only for the randomly selected process. The process is accepted with probability r_i/r_{tot}, where r_{tot} is an upper bound for the total rate. If the process is accepted, the time advances. This algorithm is not suitable when there are many processes with very low probability of being accepted and a few highly probable processes. The advantage is that if r_{tot} can be accurately estimated, only one rate r_i has to be calculated.

- Rejection-free kMC - Every time-step the list of all the possible processes is created and their rates are calculated. From the list, a process is randomly chosen. The advantage is that the process is always accepted and the time advances. The disadvantage is that the list of all the rates has to be calculated at every time-step for all the possible processes.

The rejection-free kMC is also called Bortz-Kalos-Lebowitz (BKL) algorithm [Bortz et al., 1975]. In this work, we use only the BKL version of kMC.

1.1 Bortz-Kalos-Lebowitz algorithm

In this section, we introduce the kMC model. The goal of the model is to calculate the time evolution of the simulated system. The simulation is split into subsequent states between which the simulation time t is advanced by the time-step Δt. The time-step is a function of the total rate R which is characteristic for each state of the system. The system is divided into a number of processes which cover all the possibilities which can change the system during one time-step. Each process is characterized by the partial rate R_i. The total rate is the sum of all the partial rates. Only one process is chosen for each time-step. For thermally activated processes, the rates R_i are function of the probability P_i of overcoming a barrier E_i

$$P_i \sim \exp\left(-\frac{E_i}{k_b T}\right), \tag{1.1}$$

where k_b is the Boltzmann constant and T is the simulation temperature. The probability P_i can be transformed into the rate

$$R_i = R_0 \min\left\{1, \exp\left(-\frac{E_i}{k_b T}\right)\right\}, \tag{1.2}$$

where R_0 is a prefactor which describes the amount of attempts to overcome the barrier per second. This interpretation of the prefactor means that if $E_i < 0$ the process rate should be equal to the prefactor. Hence, the minimum function is used in Eq. 1.2.

The kMC cycle can be split into the following steps:

1. Set the initial state of the system and initial starting time.
2. Determine the list of all the partial rates R_i, $i \in 1, ..., N$, where N is the number of possible processes.
3. Calculate the sum of rates $R = \sum_{i=1}^{i \leq N} R_i$.
4. Generate a random number $X \in [0, R]$.
5. Choose the process i based on criteria $\sum_{j=1}^{j<i} R_j < X < \sum_{j=1}^{j \leq i} R_j$.
6. Perform the process i.
7. Generate a random number $u_t \in [0, 1]$.
8. Advance time $t_{i+1} = t_i + \Delta t$, where $\Delta t = -\frac{\log u_t}{R}$. The Δt follows Poisson distribution with the mean value R.
9. If the end of the simulation has not been achieved, e.g., the preset total simulation time has not been reached, go back to 2.

2. Simulation of pulsed-laser deposition

The ability to control and predict growth of epitaxial thin layers is of great importance. The growth itself is governed by the kinetics of the growing species. Unlike integrated characteristics such as the coverage of each growing layer, the kinetics are difficult to extract from experiment. They can be obtained from computer simulations which can be viewed as a complement to the experiment. The experimental data are used to set the simulation parameters and then the simulations can be used to fine tune the experiment to obtain specific properties of the resulting film.

Depending on the binding energies of adatoms or molecules (hereafter we call them units), a different types of growth are achieved. Three different types of growth are usually distinguished:

- Volmer-Weber growth - the unit-unit binding energy is larger than the unit-surface binding energy. 3D islands form on the surface and grow with increasing mean thickness.

- Frank–Van der Merwe growth (Layer-by-Layer (LbL) growth) - the unit-unit binding energy is smaller than the unit-surface binding energy. In the ideal LbL growth mode, the deposited material forms a 2D layer until it is fully covered. After that, a new layer starts to grow. Note that the ideal LbL growth cannot be achieved [King and Woodruff, 1997]. In the thesis, we consider a less strict definition of the LbL growth where several not-fully-covered layers can coexist.

- Stranski–Krastanov growth - after the formation of several monolayers of units, 3D islands start to grow on the surface.

The LbL growth is often the desired growth mode in experiments and thin films preparation because it leads to homogeneous and smooth films. There are many materials for which films can be prepared by the LbL growth. A scientifically important group are so-called layered perovskites which have the same general formula ABO_3, where A and B are metal cations and O is oxygen. The A and B cations can be atoms or molecules. Depending on their composition, the layered perovskites offer a wide range of interesting properties, such as superconductivity [Maeno et al., 1994], multiferroism [Li et al., 2016], and are suitable for use in different applications such as photovoltaics [Park, 2015, Wang et al., 2019, Tailor et al., 2020].

Multiferroic materials exhibit simultaneously two of the ferroic properties, ferroelectricity, ferromagnetism, ferrotoroidicity or ferroelasticity. The combination of ferroelectricity and ferromagnetism is rarely found in nature. A material exhibiting both properties could enable significant advancements in electric-field-driven magnetic memories [Ederer and Fennie, 2008], magnetic field sensors, and tunable microwave filters [Hu et al., 2016]. Ferroelectricity is usually present for ions with empty d shells. The magnetic order is formed mostly in materials with partially filled d shells [Hill, 2000]. An example of room temperature multiferroic

that exhibits both ferroelectricity and ferromagnetism is a perovskite - hexagonal $LuFeO_3$ [Wang et al., 2013]. For epitaxial growth of single-crystalline thin films of $LuFeO_3$, the pulsed-laser deposition (PLD) is frequently used [Zhang et al., 2017, Bauer et al., 2020].

The PLD [Chrisey and Hubler, 1994] is a standard method used for deposition of metals and more complex compounds. Pulsed laser is used for repeated heating of a target from which the material for growth is evaporated. A plume of very hot atoms or molecules (units) forms and carries the material to the substrate where growth occurs. The adjustable parameters of the PLD growth are:

- Laser fluence that determines the target temperature and thus the deposition rate,
- Laser frequency that governs the length of the period between two depositions,
- Substrate temperature that affects the growth temperature and all the processes on the substrate.

The non-continuous nature of deposition and the very high temperature of impinging units and hence substrate are the main features of the PLD method and also the biggest obstacles of its simulation. Another limiting factors are the very short timescales in which a large number of units impacts the substrate and very high diffusion speed compared to the long timescales of the entire growth. In order to simulate the PLD growth, it is necessary to overcome these opposing demands on simulation time scales.

The PLD growth was investigated in situ by the X-ray scattering methods during growth and by microscopy methods when growth was completed [Christen and Eres, 2008]. Frequent in situ methods are the surface X-ray diffraction and grazing incidence small-angle X-ray scattering (GISAXS). The GISAXS method is suitable for studying the evolution of the monolayer islands growth and surface roughness development during growth [Ferguson et al., 2009]. The surface X-ray diffraction measurements are very sensitive to surface structure by measuring the scattered X-rays and they can achieve a true atomic resolution. Their very high sensitivity makes them very useful for investigation of LbL growth [Christen and Eres, 2008, Zhang et al., 2017, Vlieg et al., 1988]. The in situ methods are usually complemented by ex situ microscopy methods, e.g., atomic force microscopy (AFM) and scanning tunneling microscopy. Both methods are based on scanning the surface with a sharp tip. The resulting data give information about the surface morphology and associated parameters such as surface roughness.

A suitable model can be used to further study of the measured data. Several models based on different computational techniques were developed for PLD. One of them is the rate-equation based models [Venables, 1973, Gabriel et al., 2022b]. In this approach, a set of differential equations is solved in each time-step to determine the time evolution of layer coverages. The disadvantage of this approach is that it is not possible to calculate the morphology at a given time. On the other hand, it is possible to simulate the measured surface X-ray diffraction intensity (SXRD) time evolution.

Another possible approach is to use the kMC based model [Gabriel et al., 2020]. Unlike the rate-equations approach, the exact morphology and SXRD can

be extracted from the model at each time-step. However, the simulation time is significantly increased. In physics of thin films growth, kMC is used in a wide range of applications. A common way to simulate growth is by modelling the surface diffusion of units [Zhu et al., 2010, Zhang et al., 2008]. In this model, a diffusion barrier is present between each two cells and each unit has its own probability of diffusion at each time-step according to the current configuration of units on the surface. More complex models including the chemical processes needed to form diatomic molecules on the surface were also developed [Weckman et al., 2018]. Another possible improvement of the classical diffusion model is to simulate the entire path through plasma from the source of units to the substrate and then calculate the surface diffusion [Rashidian Vaziri et al., 2011]. However, for simulations of the perovskite growth, these two improvements are not suitable due to many possible chemical processes which can occur during growth. For the PLD growth simulations, the kMC model with diffusion of units has very limited use. So far, only very small surfaces ranging from 50×50 to 100×100 adsorption spots for submonolayer thicknesses have been calculated [Huang, 2018, Zhu et al., 2010, Zhang et al., 2008]. These scales are not sufficient for studying the SXRD evolution during growth. For such study, the substrate size has to be larger than the coherence length of the X-ray source and the simulation duration has to be long enough to include many monolayers thick growth.

In the next section, we present our kMC algorithm which overcomes the limitations mentioned above and simulate the PLD growth. First, we briefly describe the experimental setup and the available experimental dataset. We use the data measured by Eres et al. [2011] to verify the model results. Then, we use the model to describe the dependence of growth parameters such as SXRD or surface roughness on the laser frequency [Gabriel et al., 2022a].

2.1 Experiments used in simulations

The model was developed in the framework of an international collaboration between Charles University, Karlsruhe Institute of Technology (KIT) and Masaryk University focused on the PLD growth of $LuFeO_3$. Before describing the kMC model, we present the experimental constraints for the model. In order to better understand growth, it was necessary to simulate the PLD growth of hexagonal perovskites over hours of deposition time to obtain a sufficient number of grown monolayers. The model had to be preferably kMC based to replicate the measured SXRDs and to study how the PLD parameters influence growth. Due to the simulations of SXRDs, the substrate dimensions had to be larger than the correlation length of the used X-ray source which was over 1μm.

To make sure that the model is able to reproduce the measured data correctly, it had to be calibrated using the data from literature. For this task, the data published by Eres et al. [2011] were chosen because the article contains both the SXRD measurements and the information about the layer coverage which are suitable for the model calibration. The authors studied PLD growth of hexagonal perovskite $SrTiO_3$ with the deposition frequency of 0.02 Hz. During the growth, the SXRD intensity $I(t)$ was measured. The intensity can also be calculated as

a function of the layer coverages $\theta_n(t)$

$$I(t) = \left[\sum_{n=0}^{\infty} (-1)^n (\theta_n(t) - \theta_{n+1}(t))\right]^2 . \tag{2.1}$$

The authors assumed that there were at most three not fully covered layers (substrate $\theta_0 = 1$ and two growing layers θ_1, θ_2) at any time. If the lower growing layer θ_1 was fully filled, a new layer began to grow. The increase of the combined coverage of the two growing layers is equal to the number of monolayers grown per laser pulse, i.e., $\Delta\theta_1 + \Delta\theta_2 = 1/p$, where p is a number of pulses per monolayer. From the above assumptions Eq. 2.1 can be simplified to

$$I(t) = [\theta_0 + 2\theta_2(t) - 2\theta_1(t)]^2 , \tag{2.2}$$

from which the authors extracted the time evolution of coverage of each layer. Figure 2.1 shows an example of both SXRD and layer coverage calculated from the SXRD. Figure 2.2 shows the evolution of the layer coverage after one laser pulse. The calculated data are fitted by a biexponential profile with characteristic times τ_1 and τ_2, which according to the authors leads to the best fit of the data. Their explanation of the biexponential behavior was that there were two subsequent components of the inter-layer transport - fast and slow.

Based on the above results, two criteria were established to validate our kMC model. First, the model has to be able to reproduce the measured SXRD with as few parameters as possible. Second, the biexponential behavior of the inter-layer transport has to be preserved.

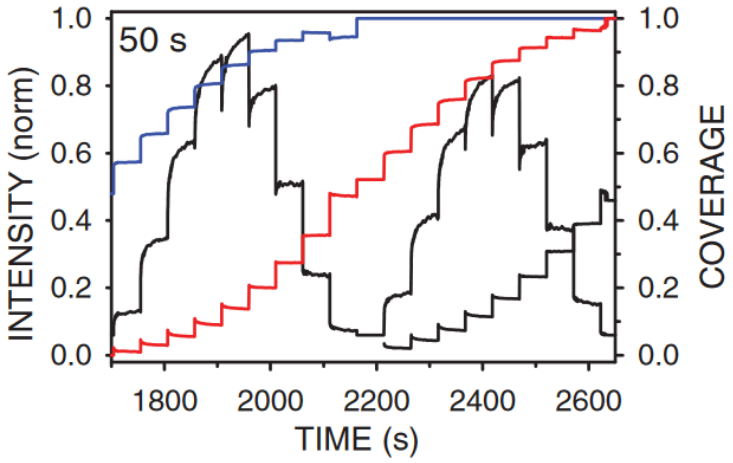

Figure 2.1: The time evolution of SXRD and the selected layer coverarages. Adopted from Eres et al. [2011].

2.2 The kinetic Monte Carlo model for simulation of the pulsed-laser deposition

The kMC method is quite frequently used for simulations of the early stages of thin films growth. Typically, models include diffusion of units on the surface.

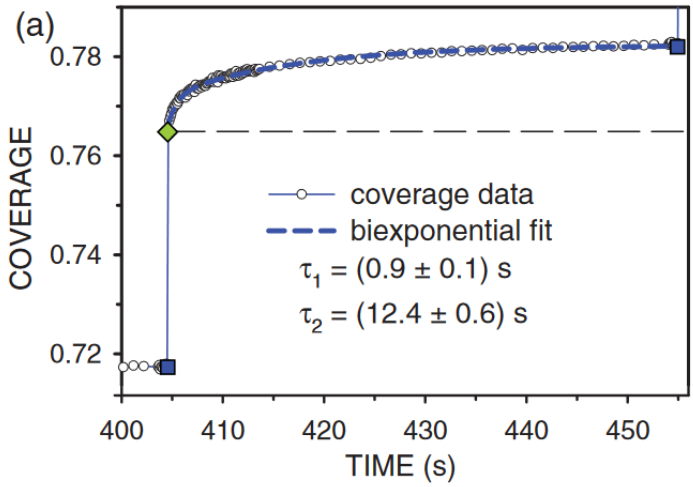

Figure 2.2: One selected coverage evolution after deposition. The dashed line shows fit of the measured data by the biexponential function with the characteristic times $\tau_{1,2}$. Adopted from Eres et al. [2011].

With this approach, however, only sub-monolayer or very small dimensions of the substrate can be simulated. To reproduce the PLD growth experiment, it was necessary to simulate at least a square with an edge length of one micrometer for approximately two hours of deposition with 5 Hz laser frequency. During deposition, more than 100 monolayers of material were deposited on the surface. Thus, the standard diffusion model was not sufficient for this application.

To overcome limitations of the diffusion kMC model, simplifications had to be made. The most fundamental simplification was to consider the system in the limit of fast diffusion and to replace diffusion by a unit gas characterized by its density on each layer. The gas acts as a source of non-condensed units. At the same time, this approximates infinitely fast diffusion because units can move between two cells on the same layer in an infinitely short time. Then, four processes were implemented (see Fig. 2.3):

- Deposition, Fig. 2.3 b),
- Condensation on the surface from the gas Fig. 2.3 c), d),
- Dissolution of condensed units back to the gas, Fig. 2.3 e), f),
- Inter-layer transport, Fig. 2.3 g).

The deposition process (Fig. 2.3 b)) is controlled only by time. After each deposition, the gas density on each layer is increased proportionally to the ratio of the uncovered area to the total area. The total number of units in each deposition is given by the deposition rate and is constant throughout the simulation.

The condensation from the gas (Fig. 2.3 c), d)) is considered to be a barrier-less process, $E_C = 0$ and thus $R_C = R_0$ (see Eq. 1.2). The probability of condensation is the same for every cell. The surface geometry is fixed during the growth, and condensation occurs on top of the existing condensed units.

The dissolution of the condensed units back to the gas (Fig. 2.3 e), f)) is a thermally activated process. For each cell, the rate of this process is determined

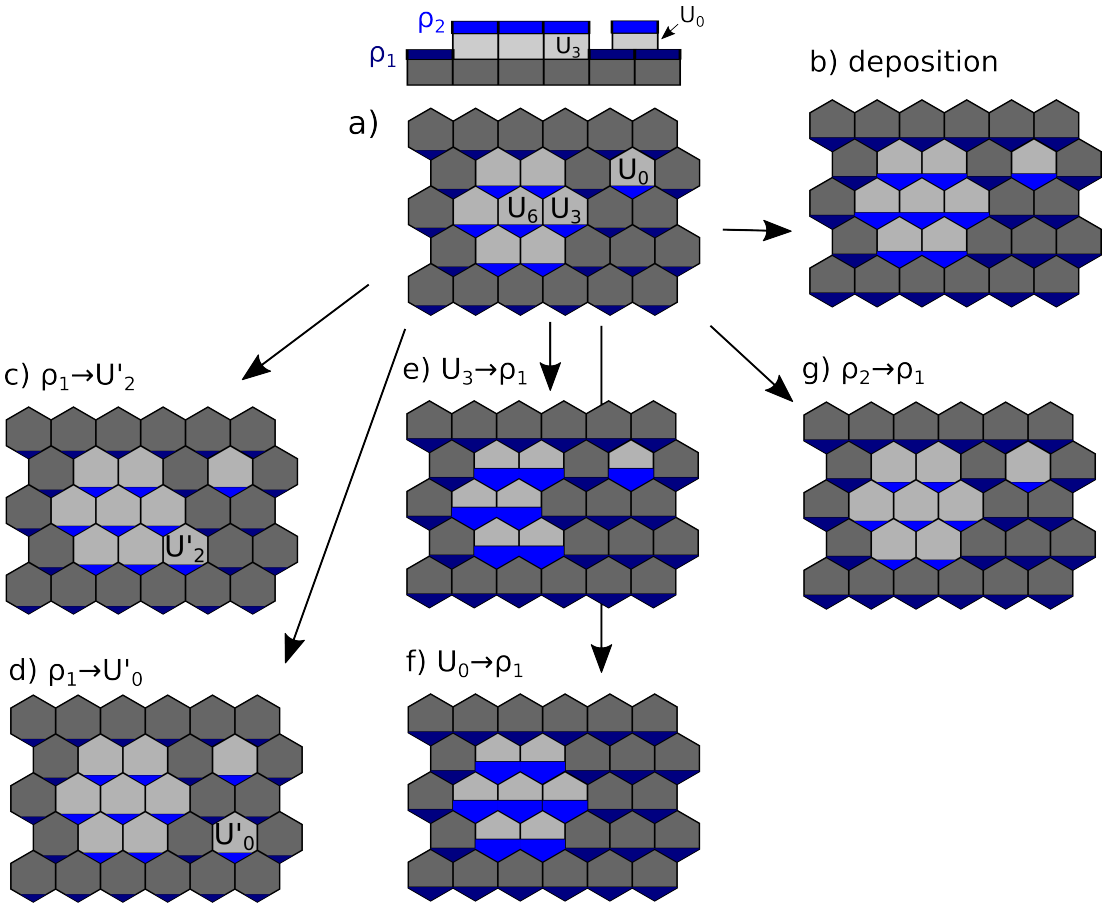

Figure 2.3: Scheme of the processes included in the model. a) is the original state with unit gas densities ρ_i on layer i represented by partially filled hexagons (blue filling) and condensed units U_j, j denotes the number of neighbors of the unit. b) shows the deposition where the density of the unit gas is increased on all the uncovered layers. c) and d) show the condensation from the unit gas which is the barrier-less process (the probability is the same for all the cells on given layer) and decreases the unit gas density on a given layer. The newly created units are denoted as U'_j. e) and f) show the dissolution back to the unit gas - its probability depends on the number of neighbors j and the dissolution increases the unit gas density on given layer. g) shows the inter-layer transport where the unit gas density is decreased on a given layer and increased on the layer below. Adopted from Gabriel et al. [2020].

by the binding energy to the lower layer or substrate E_S and by the binding energy to the unit's neighbors E_N, i.e. $E_D = E_S + n \cdot E_N$ where n is the number of neighbors.

The inter-layer transport (Fig. 2.3 g)) is a thermally activated process, the barrier of which is described by the Ehrlich-Schwoebel (ES) barrier [Ehrlich and Hudda, 1966, Schwoebel and Shipsey, 1966]; $E_J = E_{ES}$. The rate is proportional to the number of step-edge positions. Details about the model implementation can be found in Section 2.4.

2.3 Simulation results

In this section, we briefly summarize the results obtained from the model. We show that the limit of fast diffusion using the unit gas and the chosen parameters are sufficient to imitate the data from the PLD growth experiment, including the single shot time evolution of layer coverage, i.e., the inter-layer transport. We use the model to show that the apparent increase of the surface smoothness with increasing laser frequency is due to an increase of the surface temperature. The data used in this section are published in Gabriel et al. [2020, 2022a].

2.3.1 Validation of the model

To validate the model, a set of simulations with different barriers and laser frequencies was performed. Using this set, the dependence of surface roughness on morphology and laser frequency was studied.

First, we discuss the effect of barriers. A comparison of the morphologies and the corresponding SXRDs is shown in Fig. 2.4. Figure 2.4 a) shows the reference case which was calculated for the set of energies $E_S = 0.5$ eV, $E_N = 0.5$ eV and $E_{ES} = 0$ eV. The other cases are compared against it. The barrier values were chosen as low as possible to show their influence on the results. Lower E_S and E_N could not be simulated due to the rapid increase of simulation time with decreasing barriers. All the simulations shown in Fig. 2.4 were performed with the laser frequency of 5 Hz and the growth rate of 0.0135 monolayers per second (ML/s). In the reference case, the SXRD oscillates between zero and a value close to one. Together with the plotted layer coverages, it can be seen that the growth is close to perfect LbL growth. However, since the SXRD does not reach exactly one at its maximum and there is a small but visible non-zero layer coverage before the previous layer is fully filled, there is no ideal LbL growth. The morphology of the reference case shows the growth of small faceted islands which begin to coalesce. In order to simulate ideal LbL growth using the presented model, the surface and neighbor binding energies would have to be set to be as close to zero as possible. However, this barrier setup cannot be simulated in finite time.

An example of the effect of increased surface binding energy $E_S = 0.9$ eV is shown in Fig. 2.4 b). This change leads to a decrease of the size of the islands. This is due to the fact that the higher the surface binding energy, the more stable are nucleation centers consisting of one or two adjacent units. The SXRD evolution is similar to the reference case. However, the value it reaches in the peak is lower than that of the reference case. This suggests that the next layer appears earlier. Similar findings can be made when the neighbor binding energy is increased to $E_N = 0.9$ eV (Fig. 2.4 c)). In this case, the islands and the values of the SXRD maxima are even smaller than in the previous case. The effect of increased neighbor binding energy is stronger because it is multiplied by the number of neighbors in the dissolution rate calculation which is an exponential function of the barrier.

If the Ehrlich-Schwoebel barrier is introduced to the model, the resulting morphology and subsequently calculated SXRD change significantly. Figure 2.4 d) shows case with a non-zero ES barrier. In this case, the growth is clearly 3D. Naturally, the layer coverage in the right panel of Fig. 2.4 d) shows that

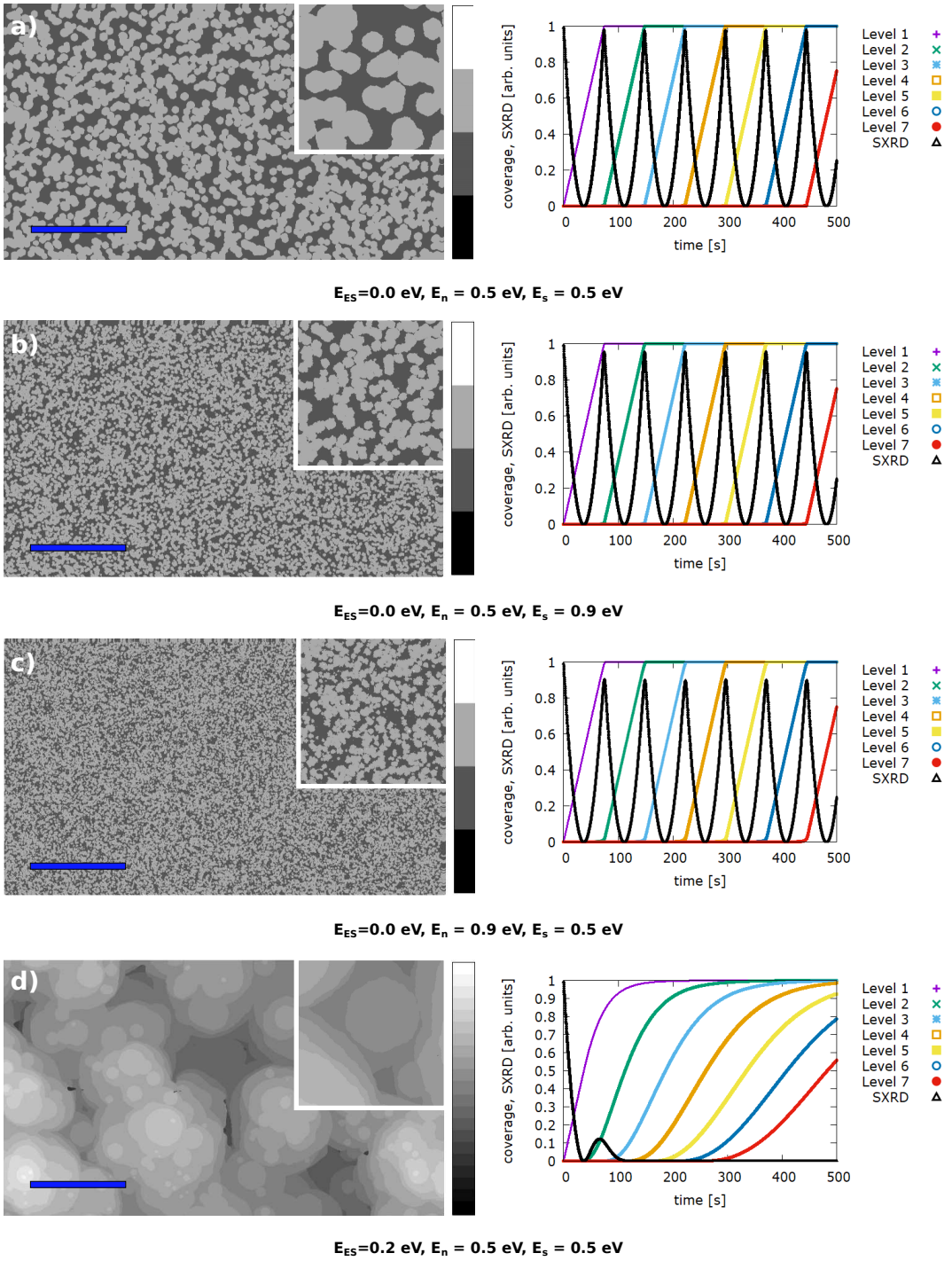

Figure 2.4: Morphologies and SXRDs for various binding energies and Ehrlich-Schwoebel barriers (listed under each case), blue line is 0.5 μm long, the size of one molecule is considered to be 0.533 nm. The size of the inset is 500 $\times$ 500 units, i.e., 266.5 $\times$ 266.5 nm. The right panels show the SXRDs (black line) and layer coverage (colored lines) evolution. Adapted from Gabriel et al. [2020].

after a certain time from the start of the simulation, many active layers grow simultaneously.

Next, we present the behavior of the model when the laser frequency is changed. In this case, the growth rate, i.e., number of monolayers per second, is

kept constant. The case where the amount of material per pulse is constant is discussed later. In this case, the deposition rate was 0.0135 ML/s. The studied laser frequencies were 5 Hz, 0.5 Hz and 0.05 Hz. The process barriers are set to be the same as in the reference case presented in Fig. 2.4 a). Figure 2.5 shows the results for the changed laser frequencies.

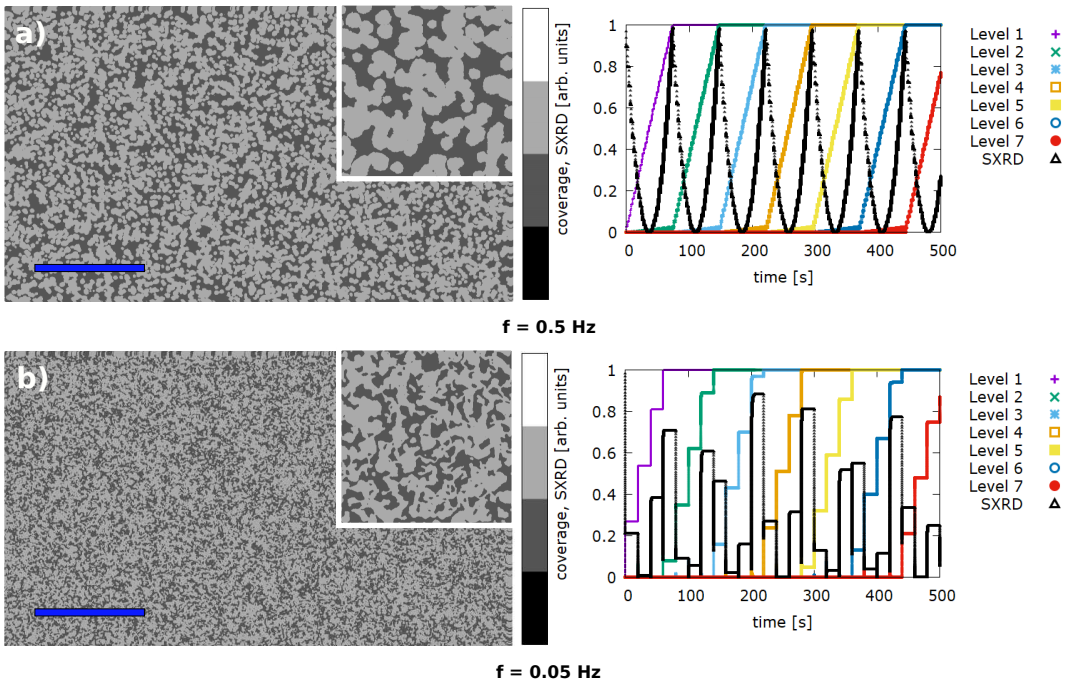

Figure 2.5: Morphologies and SXRDs for various laser frequencies (listed under each case), blue line is 0.5μm long, the size of one molecule is considered to be 0.533 nm. The size of the inset is 500 $\times$ 500 units, i.e., 266.5 $\times$ 266.5 nm. The right panels show the SXRDs (black line) and layer coverage (colored lines) evolution. Adapted from Gabriel et al. [2020].

For the laser frequency of 0.5 Hz (Fig. 2.5 a)), morphology and SXRD behavior are similar to the reference case. But there are slight differences. The islands are smaller and more connected. The SXRD has a similar time evolution, but the maxima reach lower values. In fact, the SXRD is more comparable to the SXRDs produced by increased surface or neighbor binding energy. This may be due to the fact that more units are deposited at each time-step for this laser frequency. It means that the density of free unit gas on each open layer is higher, leading to an increased probability of condensation of units next to each other and formation of a stable island. The same argument can be used to explain why the islands are smaller on average. One distinct difference from the results in Fig. 2.4 is that each layer starts growing significantly earlier. The number of deposited units on each layer is larger due to the higher number of units deposited in each pulse. Thus, the probability of forming a stable island is sufficiently high even on partially covered layers.

Decreasing the laser frequency to 0.05 Hz (Fig. 2.5 b)) leads to significantly different results compared to the previous ones. The first major difference is the completely different SXRD evolution, showing a clear pulse pattern. After each pulse, the SXRD decreases sharply and then increases even faster. The decrease

is caused by the formation of a large number of tiny islands. The increase is due to the island dissolution and reaching an equilibrium. In the equilibrium, all units are condensed on the surface and bound to a sufficient number of neighbors. The SXRD shows that the equilibrium is reached rather fast, in a few seconds. The second significant difference from the previous results is in morphology. Note, that the deposition rate 0.0135 ML/s means that about 0.27 ML of units are deposited per pulse. The gas density on each layer is very high and thus there is a high probability of forming a large number of stable nucleation centers. Hence all the units are bound to other units before they are able to form circular faceted islands as in the previous cases.

2.3.2 Simulations of inter-layer transport

Eres et al. [2011] studied growth of $SrTiO_3$ using PLD. From the SXRD measurements, the authors were able to extract the time evolution of a single layer during growth. Figure 2.2 shows an example of the time evolution with a biexponential fit

$$\theta(t) = A_1 \exp(-(t - t_0)/\tau_1) + A_2 \exp(-(t - t_0)/\tau_2) \tag{2.3}$$

with the time constants $\tau_1 = (0.9 \pm 0.1)\,\mathrm{s}$ and $\tau_2 = (12.4 \pm 0.6)\,\mathrm{s}$ and constants A_1, A_2. Since two different time constants are involved, the authors conclude that there are two types of the inter-layer transport – slow and fast – each operating on different timescales.

Using our model, we provide an alternative explanation that there is only one inter-layer transport process which is driven by the dissolution of weakly bound units (units with less than two neighbors) and subsequent transport to lower layers. We hypothesize that the time constants of the biexponential behavior are tightly connected with the barriers used in the model.

To prepare the simulations, all the necessary model parameters had to be determined. First, the temperature T, laser frequency f, and deposition rate D were set to the same value as in Eres et al. [2011], i.e., $T = 940$ K, $f = 0.02$ Hz, $D = 0.083$ ML/s. Second, the jump to lower layer was considered barrier-less - the Ehrlich-Schwoebel barrier $E_{ES} = 0$ eV. Finally, the surface and neighbor binding energies (E_S and E_N) were calculated using the time constants τ_1 and τ_2 determined from the measured data, assuming that the ES barrier is not present. In this case, the jump is almost instantaneous, and the energies can be obtained from

$$\tau_1^{-1} = R_0 \exp\left(-\frac{E_s}{k_b T}\right), \tag{2.4}$$

$$\tau_2^{-1} = R_0 \exp\left(-\frac{E_S + E_N}{k_b T}\right). \tag{2.5}$$

By solving these relations, we found the following values of the energy barriers: $E_S = 2.05$ and $E_N = 0.2$ eV.

The results with this barrier setup are presented in Fig. 2.6 a). The time span of both SXRD and layer coverage is the same as in Fig. 2.2, which shows the experimental data. The simulated SXRD agrees well with the experimental data. The small differences may be due to the unknown state of the substrate at the start of the experiment (whereas the substrate is completely flat at the beginning

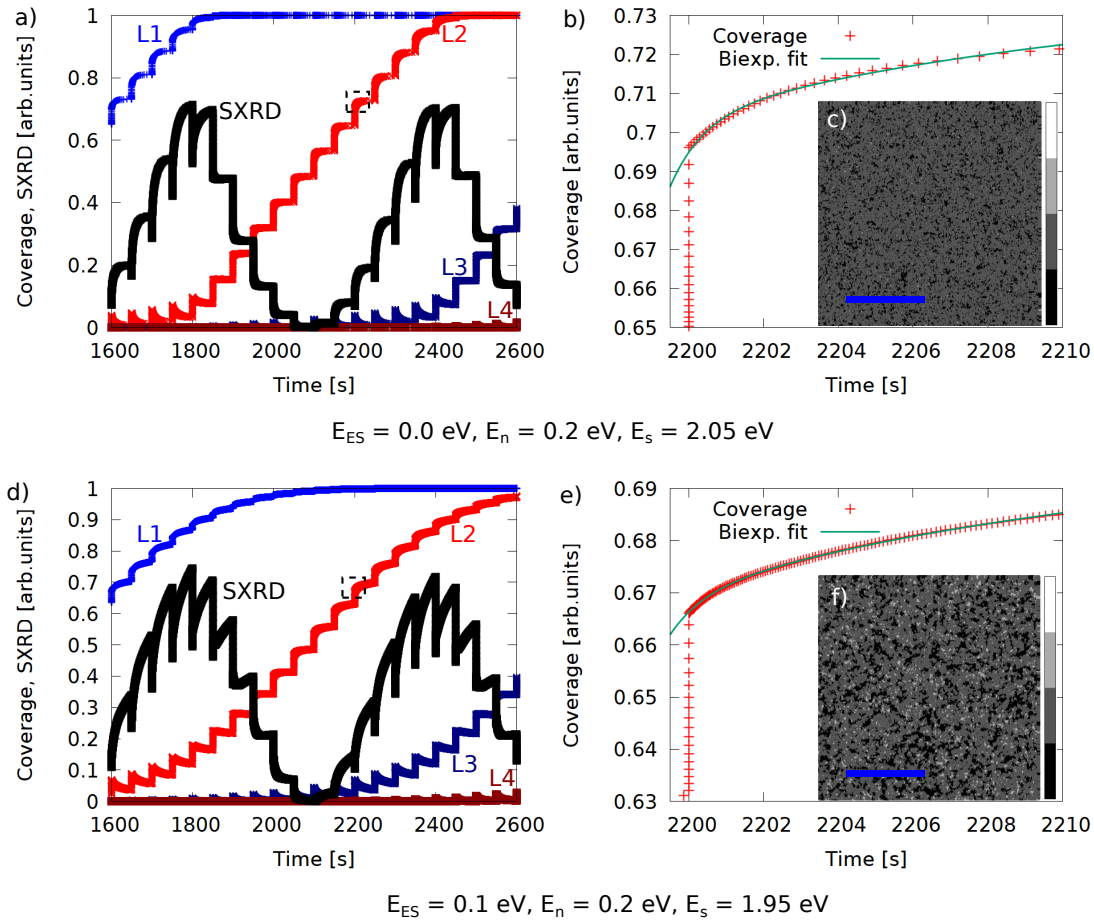

Figure 2.6: a), d) The simulated SXRD for the same part of deposition as in Fig. 2.1. The L1–L4 mark four different growing layers. The dashed square indicates the part of the data shown in the detail of single shot transient of the layer coverage increase after deposition (b) and e)) with the biexponential fit proposed by Eres et al. [2011]. c), f) The sample morphology obtained from the simulation. The blue bar indicates 100 nm. Adopted from Gabriel et al. [2020].

of the simulation). The layer coverages are also in very good agreement with the experimental data.

The time evolution of the layer coverage after one pulse is shown in Fig. 2.6 b). The associated step is marked with the dashed square in Fig. 2.6 a). The coverage data were fitted by the biexponential function 2.3 with the time constants τ_1 and τ_2 set to the same value as in the experiment. The only free parameters were the scaling constants A_1 and A_2. The fit describes the simulation results very well. Therefore, the biexponential behavior can be obtained using the kMC model without any assumptions about the inter-layer transport processes. The fast and slow processes proposed by Eres et al. [2011] could be dissolution of weakly bound units and their jump to the lower layer. The two different timescales are then given by the surface and neighbor binding energies.

However, there is some ambiguity in the energy barriers. If the ES barrier is considered nonzero and the neighbor binding energy is decreased accordingly, the SXRD and layer coverage profile look like in Figs. 2.6 d) and e), where a small ES barrier is introduced. However, the introduction of the ES barrier has significant

effects on the resulting morphology (compare Fig. 2.6 c), f)). When the ES barrier is present (Fig. 2.6 f)), the islands are significantly smaller. To obtain the model parameters including the ES barrier, other morphological characteristics would have to be known from the experiment, such as the evolution of average island sizes or surface roughness. With these data, it would be possible to tune the model parameters to successfully replicate all the SXRD, inter-layer transport behavior and morphology.

2.3.3 PLD growth of $LuFeO_3$ – experiments used for kMC simulations

After the model was tested, it was used to improve our understanding of the experimentally measured data. The experiment was performed at the PLD facility in KIT. $LuFeO_3$ was grown on yttria-stabilized zirconium using four different laser frequencies $f = 1$, 2, 3, and 5 Hz. After the growth was completed (approximately 140 monolayers), images of the resulting surfaces were taken using AFM (Fig. 2.7).

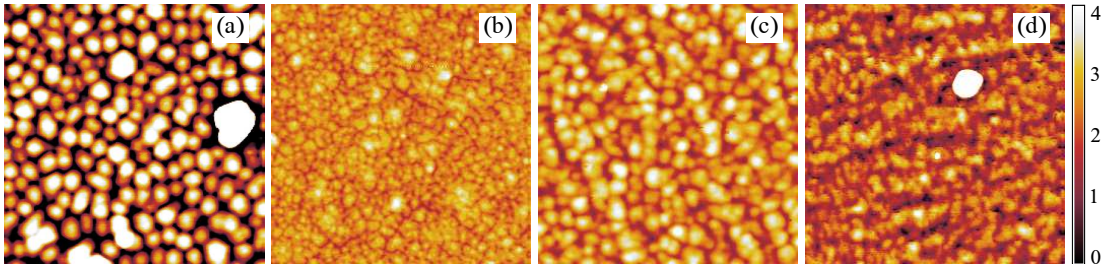

Figure 2.7: AFM images of morphologies for frequencies (a) 1 Hz, (b) 2 Hz, (c) 3 Hz, and (d) 5 Hz. The colorbar denotes the height in nanometers, the lateral image size is 1 μm. Adopted from Gabriel et al. [2022a].

All the samples are very smooth. The maximum measured height difference is 4 nm and the root mean square roughness is 1.5 nm (1 Hz), 0.4 nm (2 Hz), and 0.6 nm (3 Hz and 5 Hz). For the 1 Hz laser frequency, the grains are protected from coalescence by deep valleys. Steps on the surface are present for the 3 Hz and 5 Hz samples.

Black line in Fig. 2.8 a) shows the in situ measured SXRDs for each frequency. The colored lines in Fig. 2.8 a) show the calculated SXRD reconstructions

$$I(t) = \text{const} \cdot \left| \sum_{j=1}^{N} \theta_j(t)(-1)^j \right|^2, \tag{2.6}$$

obtained under the assumption that the j-th layer coverage $\theta_j(t)$ can be approximated by hyperbolic tangent

$$\theta_j(t) \sim \frac{1 + \tanh\left(\dfrac{t - t_j}{w_j}\right)}{2}, \tag{2.7}$$

where t_j is the time at which the j-th layer is half-filled and w_j is the $\theta_j(t)$ profile width. The reconstructed SXRD matches well the original SXRD. Hence, we

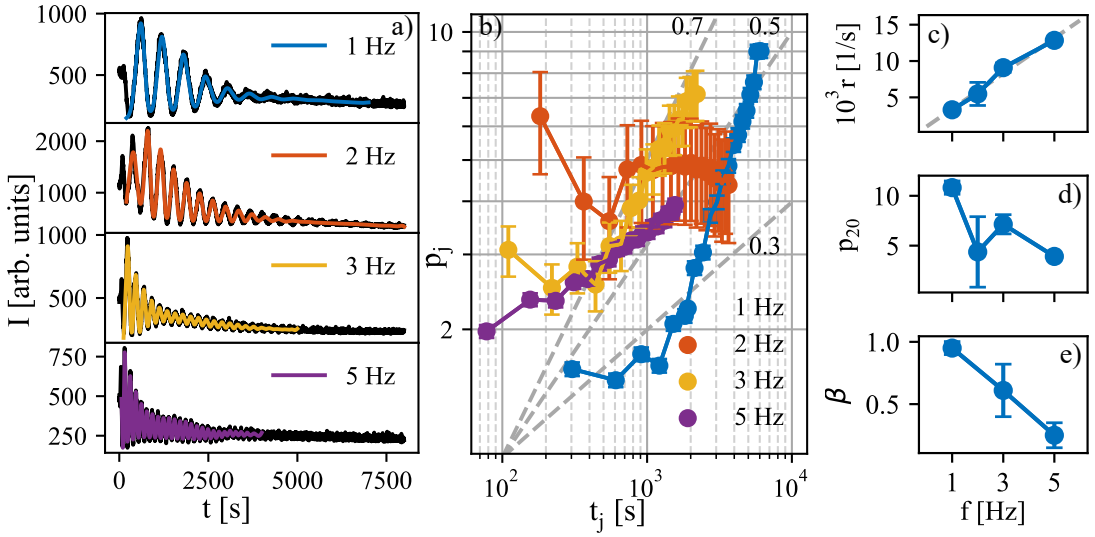

Figure 2.8: a) In situ measured SXRDs for four laser frequencies 1, 2, 3, and 5 Hz. For each, the first 20 hyperbolic tangent profiles were fitted (colored lines) (Eq. 2.7). b) The relative widths p_j of the hyperbolic tangent profiles and their time evolution. The dashed lines denote dependence t^β, $\beta = 0.3, 0.5, 0.7$. c) The growth rate r. d) The width of 20th profile p_{20}. e) The growth exponent β as a function of the laser frequency. For $f = 2$ Hz the exponent could not be determined. Adopted from Gabriel et al. [2022a].

assume that the calculated coverages are close to the real ones. Figure 2.8 b) shows the time evolution of relative profile widths $p_j = w_j r_j$, where $r_j = 1/(t_j - t_{j-1})$ is the growth rate. The denominator is the time elapsed between the half-filling of two subsequent layers.

The scaling of the subsequent profile widths p_j was found to obey a power law, i.e., $p_j \sim t^\beta$ (Fig. 2.8 e)). β is a critical exponent called the growth exponent and describes the interface width which is directly related to roughness [Barabási and Stanley, 1995]. For less than monolayer thick, the Poisson growth dominates and $\beta = 0.5$. The interface width grows as t^β until the saturation time t_x is reached. Then the interface width remains constant for the rest of the growth and is called the saturation width $w_{sat}(L)$. Its dependence on the size of the simulation system L follows the power law $w_{sat}(L) \sim L^\alpha$, where α is the second critical exponent called roughness exponent. The third critical exponent is the dynamic exponent z, which describes when the system reaches the saturation time $t_x \sim L^z$. It can be shown that $z = \dfrac{\alpha}{\beta}$ [Barabási and Stanley, 1995].

2.3.4 PLD growth of $LuFeO_3$ – kMC simulations

To further study the influence of the laser frequency, the presented kMC model was used. The model parameters were set as in the experiment, i.e., the laser frequencies $f = 1$, 2, 3, and 5 Hz; growth temperature $T = 850$°C. From the distance between two SXRD peaks, the deposition rate was determined to be 0.00258 ML/pulse. The simulation time was equivalent to 40000 laser pulses. The last set of parameters were the neighbor and surface binding energies and

ES barrier. In order to determine them, an extensive set of simulations was made for the laser frequency $f = 5$ Hz to find the best SXRD match.

The simulated and experimental SXRD envelope functions were compared to determine the match. First, the decreasing trend at the beginning of the growth had to be removed from the measured data. This decrease is not physical and is caused by the slight shift of the detector in the experimental setup. The trend removal was done by subtracting the moving average of the data and removing the first peak to reduce the influence of the substrate. Then, the local maxima and minima were found and fitted by exponential functions. The characteristic decay time obtained from the fits was compared with the simulated data which were processed in the same way as the experimental data. The final set of parameters is as follows: $E_N = 0.66$ eV, $E_S = 1.30$ eV, $E_{ES} = 0.135$ eV. The results obtained for this set of parameters are presented in Fig. 2.9. The evolution of the layer coverages (Fig. 2.9 a)) shows an increase of the widths of the subsequent profiles. Figure 2.9 b) presents the simulated SXRD obtained from the layer coverages using Eq. 2.6 and is compared with the measured SXRD (Fig. 2.9 c)). Figure 2.9 d) shows the resulting morphology after the the simulation is completed. The behavior of the selected layer coverage after the pulse is in inset Fig. 2.9 e). Right after the deposition, the coverage sharply increases. Then, it slowly decreases until the next deposition of units occurs. The decrease is the result of dissolution and jumps of units to lower terraces.

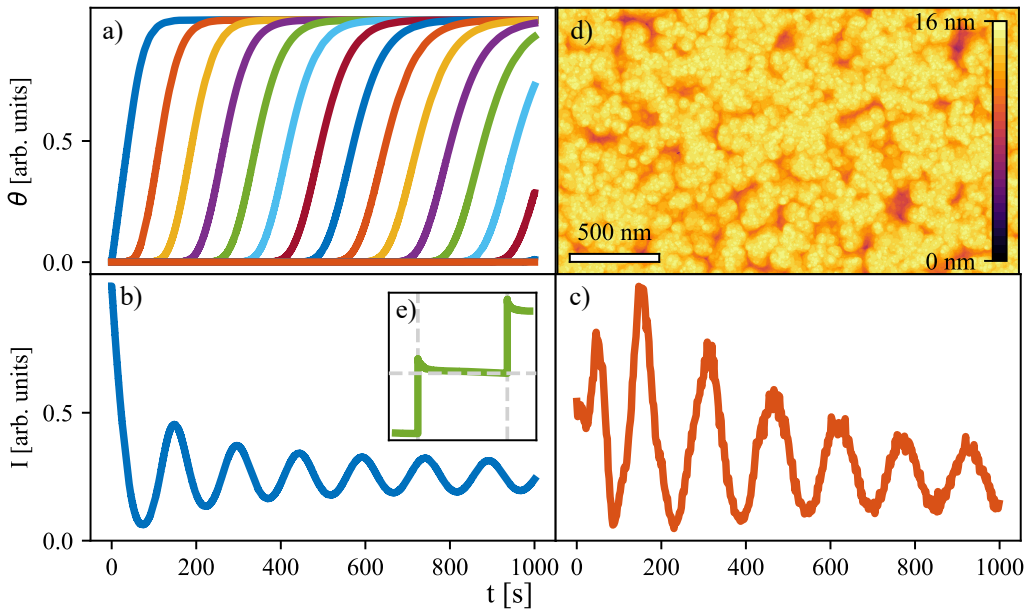

Figure 2.9: a) The time dependencies of layer coverages for the first 1000 seconds, b) the simulated SXRD, c) the experimentally measured SXRD, and d) the resulting morphology at the end of the simulation (8000 seconds). The inset e) shows behavior of the layer coverage after one pulse, the vertical dashed lines mark the deposition times and the horizontal dashed line marks the layer coverage at the last point before the next pulse. Adopted from Gabriel et al. [2022a].

The obtained set of parameters was used for all the simulations for different laser frequencies. Figure 2.10 shows the simulation results comparable to the

measured data in Fig. 2.8. Figure 2.10 a) contains the simulated SXRDs for each frequency. Note, that the vertical axis scale is different compared to Fig. 2.8 a) which is due to the different scaling constant (see Eq. 2.6). The subsequent profile widths are in Fig. 2.10 b). Figure 2.10 c) shows the width of 20th profile p_{20} and in contrast to Fig. 2.8, the panel showing the growth rate r is not present because it is fixed in the simulations.

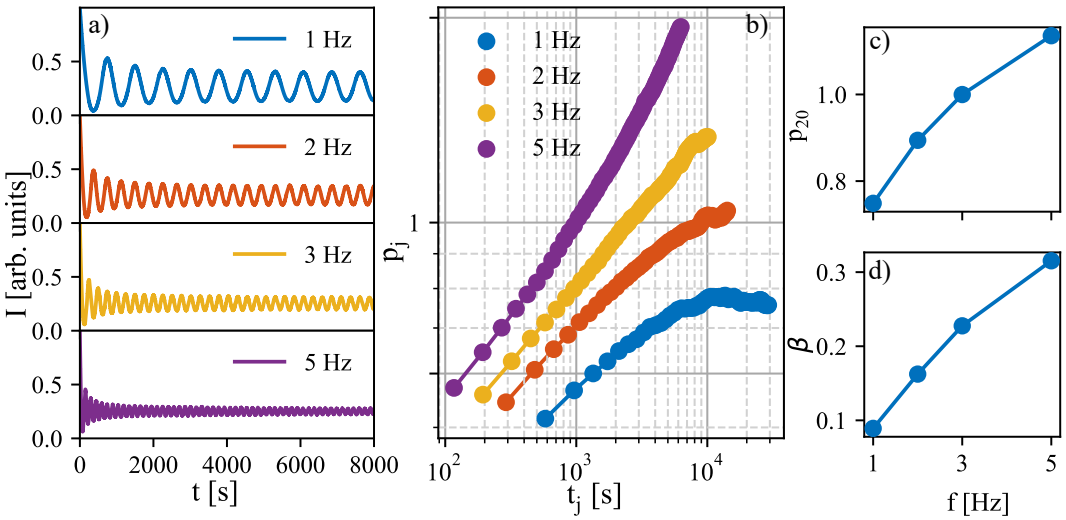

Figure 2.10: a) The SXRDs for simulations with different laser frequencies f = 1, 2, 3, and 5 Hz. b) The relative widths of individual layer coverages fitted by hyperbolic tangent profiles. c) The characteristic profile width p_{20} as a function of frequency and d) the evolution of β with frequency. Adopted from Gabriel et al. [2022a].

In the following section, we compare the experimental data (Fig. 2.8) with the data obtained from the simulations (Fig. 2.10). An important note which is necessary to understand the similarities and differences between these two data sets is that model parameters were determined for the laser frequency $f = 5$ Hz.

We start by comparing the scaling exponent β behavior (Fig. 2.8 e) and Fig. 2.10 d)). For $f = 5$ Hz, β has similar values in both the experiment and simulations. For lower frequencies, however, its behavior is significantly different. In the simulations β decreases, i.e., the surface is smoother, while in the experiment β increases. The explanation of this model behavior can be seen from Fig. 2.9 e). In the simulation, the layer coverage is not static during the pulses, the units tend to dissolve until the next plume of material arrives. This effect is physical, i.e., it is determined by the rates of dissolution of weakly bound units, and it is stronger the longer time period between pulses is. As the laser frequency decreases, the system gets closer to equilibrium before the next pulse. This effect leads to smoother surfaces. The same behavior as for the scaling exponent β can be observed for the characteristic profile width p_{20} (Fig. 2.8 d) and Fig. 2.10 c)). Again, the slope of p_{20} in the experiment and in the simulations are also completely opposite. For 5 Hz laser frequency, the SXRDs are similar in the simulations and experiment. Several gradually decreasing oscillations occur before the SXRD becomes a straight line with small fluctuations. However, for the

lower frequencies, the SXRDs are again very different. For 1 Hz laser frequency, the simulated SXRD oscillates for the entire time period shown which is opposite to the experiment where the SXRD is close to that measured for 5 Hz laser frequency.

The comparison of the simulated and measured data indicates that the laser frequency itself is not the governing factor which drives the experimentally observed decrease of roughness for higher laser frequencies. This factor can be determined from the model parameters, assuming that the model has all the parameters necessary to simulate such behavior.

The results obtained from the model depend on the rates of the individual processes since these determine which process is chosen at each time-step. The rates depend on the constant prefactor and ε_i (see Eq. 1.2 where $\varepsilon_i = -E_i/(k_b T)$). Based on the previous findings, the exponent ε_i changes with the laser frequency f. If it was constant, the simulated and measured behavior of β would be the same. ε_i is a function of the Boltzmann constant and two variables - the energy barrier E_i and the growth temperature T. We assume that there is no physical reason why the energy barriers E_i should depend on f. If the opposite were true, it would mean that the most fundamental processes on the surface are dependent on some external events. After eliminating the parameters that cannot be affected by the laser frequency, the only remaining parameter is T, which is set in the experiment.

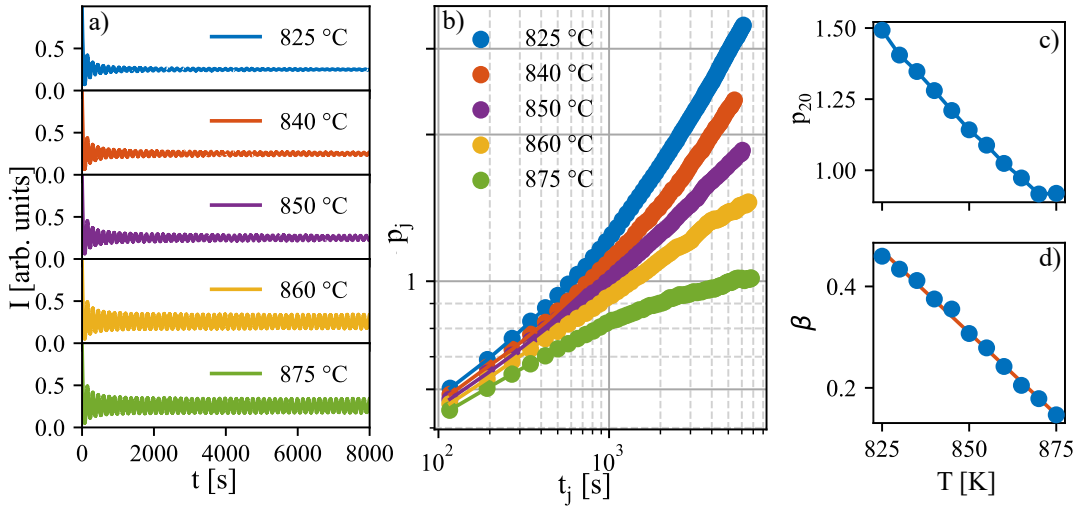

Figure 2.11: a) The SXRDs for simulations for chosen temperatures T = 825, 840, 850, 860, and 875°C. b) The relative widths of individual layer coverages fitted by hyperbolic tangent profiles. c) The characteristic profile width p_{20} as a function of temperature and d) the evolution of β with temperature. Adopted from Gabriel et al. [2022a].

We propose that the increase of growth temperature drives the experimentally observed decrease of surface roughness. To prove this idea, we performed a study similar to that presented in Fig. 2.10, but with variable temperature. The results are shown in Fig. 2.11. The first supporting argument for this idea can be derived from Fig. 2.11 d). The figure shows that the scaling exponent β decreases with increasing growth temperature. If we compare Figs. 2.11 a) and 2.10 a), we can

see that the increase of temperature has a similar effect to the decrease of laser frequency. This is in agreement with previous findings that longer time between pulses (or generally higher rates which technically scale each time-step and allow more processes in the same time period - see Eq. 1.2) leads to the decrease of surface roughness.

In the experiment, the temperature is usually set on the back side of the substrate using a thermocouple or laser heating. This arrangement does not guarantee that the front side where the film grows will have the same set temperature. Especially for PLD, the impinging units are significantly hotter than the substrate. The heat of the impinging units can significantly increase the surface temperature which is the true growth temperature. Using our simulations, we determined the difference between the "experimental" and "true" temperatures for the case where the laser frequency is $f = 5$ Hz. For this study, we repeated the model parameter determination procedure used in the case of $f = 5$ Hz for $f = 1$ Hz.

The effect of the temperature is demonstrated in Fig. 2.12. Both Figs. 2.12 a) and b) are split into two halves. The results of simulations with the parameters obtained from the experiment for $f = 5$ Hz is in the upper and for $f = 1$ Hz in the lower half. The SXRDs and morphology comparisons are shown in Fig. 2.12 a) and Fig. 2.12 b), respectively. It can be seen that the growth is much more different from the LbL growth in the lower set of figures. If we compare these data with those in Fig. 2.11, we see that the $f = 1$ Hz and $f = 5$ Hz cases are similar to the cases with low and high temperature, respectively. From the obtained barriers, we determined that the effective temperature increase is about 7 % for $f = 5$ Hz. Because the rates are an exponential function of temperature, the increase of process rates is much more pronounced - the rate of jump down increases by about 9 %, the rate of dissolution of units without neighbors increases approximately 2.5 times and with one neighbor approximately 3.75 times.

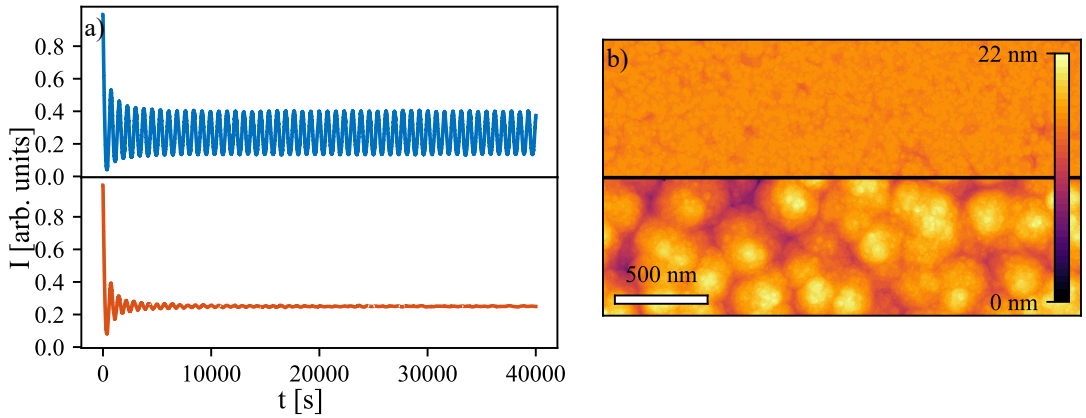

Figure 2.12: a) The comparison of SXRDs and b) morphologies for the nominal temperature obtained from 5 Hz experimental data (upper half) and for the corrected temperature obtained from 1 Hz experimental data (lower half). Adopted from Gabriel et al. [2022a].

The dependence of the surface roughness and the average island diameter on the temperature and laser frequency is in Fig. 2.13 a) and b), respectively. The

roughness behavior confirms our previous findings deduced from the behavior of the scaling exponent β, i.e., the roughness decreases with increasing temperature and increases with increasing laser frequency. This finding is consistent with the example shown in Fig. 2.9 e). The layer coverage reaches equilibrium throughout the time period between two pulses. If the temperature is increased and the laser frequency is decreased, the system gets closer to equilibrium before the next pulse. The average island size is calculated by autocorrelation of the given surface and determination of the correlation length. The dependence of the correlation length on both parameters is similar to that of the roughness.

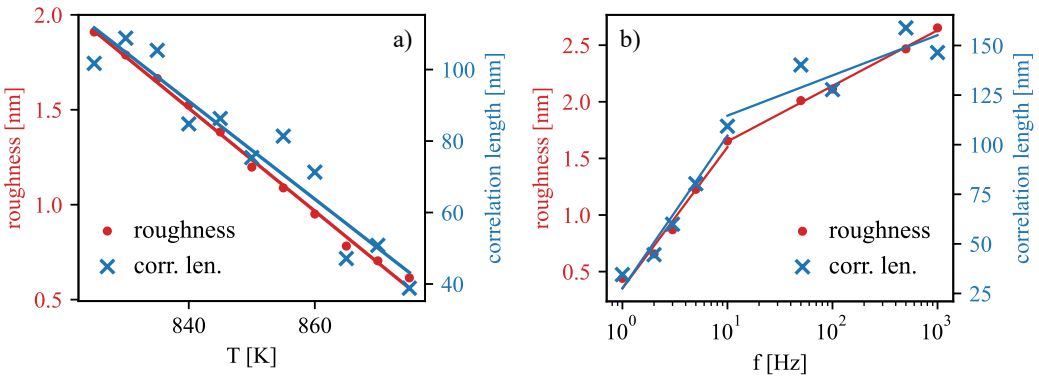

Figure 2.13: Dependence of the simulated roughness and correlation length on temperature a) and laser frequency b). The lines are guides for the eye. Adopted from Gabriel et al. [2022a].

In this chapter, we presented the kMC model for simulations of the PLD LbL growth. We tested the model using the data from literature and applied it to the data measured by the research group at KIT. We used the model to provide an alternative explanation of the characteristic times of the inter-layer transport. We found that the previously proposed solution with two competing mechanisms of the inter-layer transport can be simplified if dissolution of units and their subsequent jump to a lower layer are considered. Moreover, we found that the effect of substrate heating may be responsible for the experimentally observed decrease of surface roughness. This effect can be demonstrated by calculation of the scaling exponent β. To fully understand and quantify this, we also calculated the dependence of the surface roughness and average island diameter on temperature and frequency.

2.4 Implementation details

The standard kMC model for simulations of thin films growth includes the diffusion of more or less mobile units on the surface. A more detailed approach

includes the kinetics of atoms, their chemical reactions and bond formation. The main issue of the standard models is their time complexity.

The time complexity is caused mainly by the large number of atoms for which diffusion has to be simulated. The diffusion itself is a random walk of atoms which means that many steps are needed to reach a stable configuration. This effect is stronger the higher the adatoms temperature is. Additionally, Maksym [1988] showed that when diffusion is included, the best achievable scaling of the kMC selection algorithm is $N^{3/2}$.

In order to simulate sufficiently large simulation domains, both these obstacles have to be overcome. First, we address the "diffusion problem". The solution and introduction of the unit gas was described in detail in Section 2.1. The unit gas approach removes the necessity to simulate many steps of random walk where the unit goes back and forth in a very limited space, only slowly reaches another unit with which it can create a stable nucleus. The existence of the unit gas and the condensation and dissolution processes allow units to form stable nuclei faster because the speed of diffusion is unlimited. At the same time, the kMC nature of the model is preserved because the places where the units condense or from which they dissolve are chosen randomly. The fact that the unit gas is shared by all the terraces with the same height, regardless of whether they are connected, also helps units to find neighbor faster, especially in cases where the ES barrier is high (jump to lower layer is limited) and very few units are randomly walking on the terrace. In this case, the elapsed simualation time moves very slowly because the rate of a single diffusing unit can be very high, especially for PLD, as the rate is a function of temperature.

The second issue was overcome by building a data structure in which all the information is stored in a way that allows a constant event selection time no matter how large the domain is. Hence, all the scaling is caused by simple dependence "larger domain $\Rightarrow$ more units added to the system after every deposition $\Rightarrow$ more processes occurring".

In the following lines, we explain the implementation of the model in the situation where each unit has six neighbors. The model can be easily modified to simulate any structure as long as it does not change during the simulation. The model was implemented in C++ language using only standard libraries.

First, the substrate is divided into cells c_i (Fig. 2.14 a)) following the prescribed geometry. These cells are numbered from one to N by indices i, where N is the total number of cells. The index is denoted by a shade blue in Fig. 2.14 a). For each cell, a list with the indices of neighboring cells is created. This method allows us to quickly find a neighbor of neighbor and modify its properties. Each cell also contains information about its height h, i.e., the number of condensed units at a given cell with coordinates x, y on the substrate, and the number of neighbors n for which $h_i \leq h_a$, $a \in$ neighbors list.

A secondary structure to calculate the rates of each process is created (Fig. 2.14 d)). The data are grouped into a 3D matrix M_{hnj}. The first index groups all the cells with height h, the second index number of neighbors n, and the third index j where the index of the cell i is stored.

At the start of the simulation, all the cell indices are stored in M_{06j} because their height is zero and they have six neighbors each. For now, the indices i and j coincide. After the first deposition when the first unit condenses on the surface

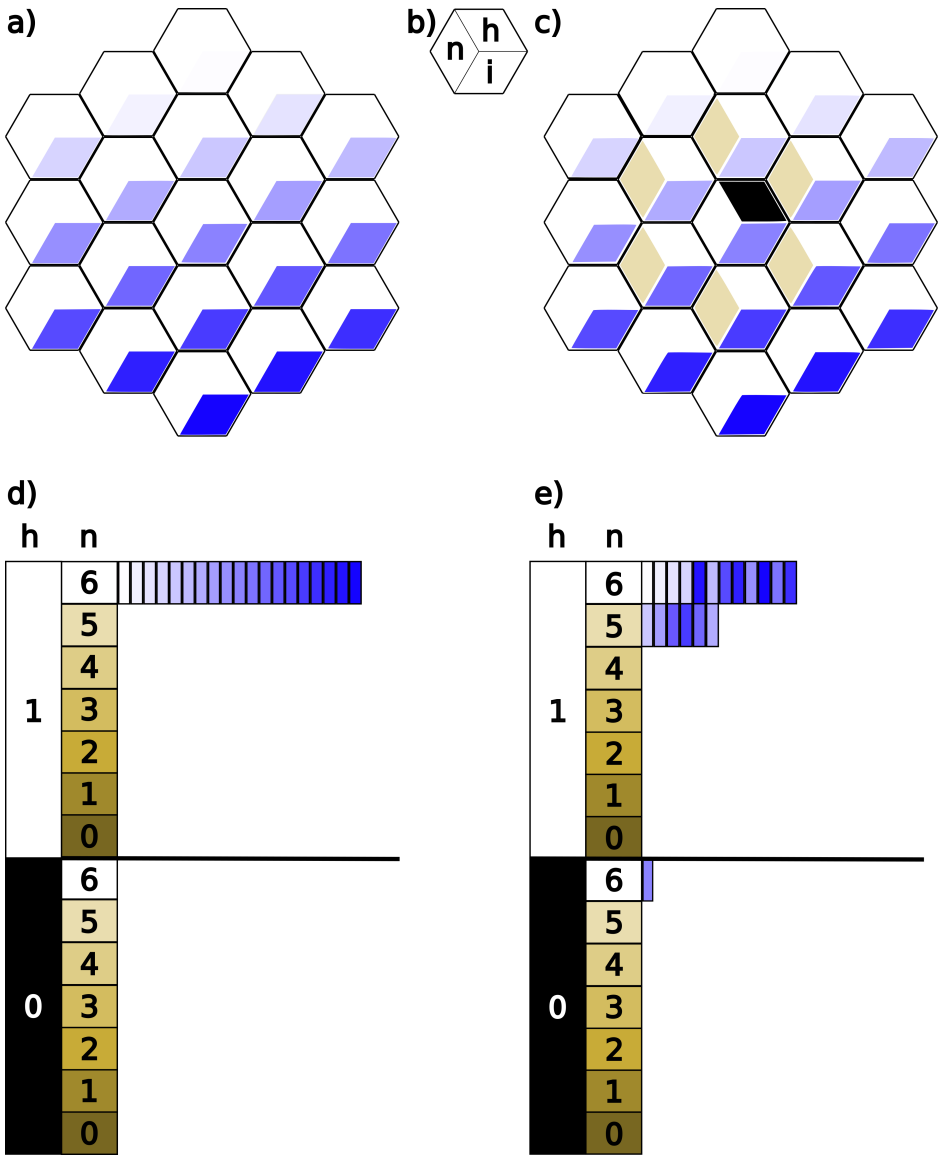

Figure 2.14: The visualisation of the data structure in the model. a), c) The hexagonal grid represents the substrate geometry. b) Each hexagonal cell is split into three parts which are stored in it - the number of neighbors at the same or higher layer (n; left third), the height, i.e., the number of condensed units in given cell (h; top third) and the index where the cell in the data structure (i, bottom third). a) and d) show the state before dissolution of an unit. c) and e) show the state after an unit dissolves in the central cell. After the dissolution the height value of the cell decreases and the number of neighbors are recalculated for the central cell and its neighbors. In the second structure (d) and e)) which is used to determine which process is chosen at each time-step this is represented by moving one cell from the original state ($h = 1$, $n = 6$) to ($h = 0$, $n = 6$). The neighboring cells are moved to ($h = 1$, $n = 5$). The index position after the move in ($h = 1$, $n = 5$) is given by moving the cell one-by-one clockwise starting from the cell above the one in which an unit dissolves. The indices in the original state ($h = 1$, $n = 6$) are given by swapping the index of the last cell in the list with the moved cell. The new last cell (the moved cell) is then removed from the list.

in cell c_k (its height increases to one), the index k is moved to M_{100} (there are no units with $h = 0$ and hence $n = 0$). Its neighbors are kept inside M_{06j}. From now on the indices i and j do not coincide because instead of keeping empty cell in M_{06j} the last index ($j = N - 1$) is swapped with the index k. The k index which is now the last index is removed from M_{06j}. The index j is also stored in the cell c_i. Moving the cell indices i in the matrix M_{hnj} is performed after every time-step. Figure 2.14 shows example how the indices are shifted after dissolution from a surface where all the cells are on the same height ($h = 1$). In this case the indices of neighbors are moved from M_{16j} to M_{15j} because they have one less neighbor which satisfies the condition of neighbor (see above).

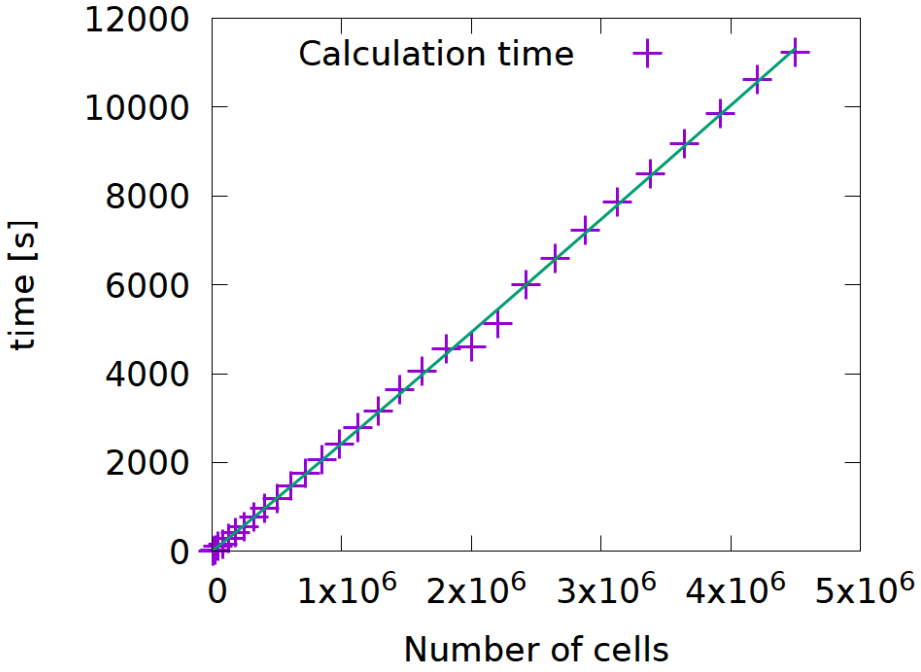

Figure 2.15: The dependence of computational time on the number of cells. Adopted from Gabriel et al. [2020].

Setting the structure this way and using the build-in constant time complexity function in the C++ language vector.size() which returns the number of elements in the array, we are able to obtain the total rate R of all the processes at each time-step with constant time complexity. For example the total rate of the dissolution process R_d can be obtained by

$$R_D = \sum_{h=0}^{h>h_{max}} \sum_{n=0}^{n\leq 6} \left[M_{hn}.\text{size}() \cdot R_0 \exp\left(-\frac{E_S + nE_{N'}}{k_b T} \right) \right]. \tag{2.8}$$

The $E_{N'}$ denotes the neighbor binding energy. The other two processes can be calculated in the same way by multiplying by corresponding exponential function. The bounds of the sums are independent of the substrate size. Figure 2.15 shows the time necessary for the whole simulation as a function of the number of cells. The data are fitted by curve $f(x) = a \cdot x^b + c$ with $b = 1.026$.

Hence, the following are always stored in memory and updated at each time-step:

- total rate R
- total rates of each process R_A (condensation R_C, dissolution R_D and jump down R_J)
- rates of each process for each current height $R_{A;h}$
- rates of each height and each number of neighbors $R_{A;hn}$ (see for example for dissolution Eq. 2.8 without the sums over h and n, similarly for $R_{A;h}$)

The event selection procedure is as follows:

- Generate random number $X \in [0; R]$
- Choose process $A \in \{C = \text{condensation}, D = \text{dissolution}, J = \text{jump down}\}$ based on cycle:

```
for A ∈ {C, D, J}:
    if X − R_A < 0:
        return X, A
    else:
        X = X − R_A
```

- For selected process A select height h_0:

```
for h ∈ [0, h_max]:
    if X − R_{A;h} < 0:
        return X, h
    else:
        X = X − R_{A;h}
```

- For selected process at selected height $A; h_0$ select for which number of neighbors the process will happen:

```
for n ∈ [0, n_max]:
    if X − R_{A;hn} < 0:
        return X, n
    else:
        X = X − R_{A;hn}
```

- Obtain the searched index j:

$$j = \text{Trunc}\left(\frac{X}{R_0 \exp(\cdots)}\right)$$

where Trunc is a truncation function and $\cdots$ denote the argument of the exponential function based on the selected process.

3. Simulation of polaronic diffusion

Polaron is a quasiparticle formed by the interaction of a charged particle (electron or hole) and crystal vibrations in a polarizable material [Franchini et al., 2021]. Polarons can be either localized (small polarons) [Holstein, 1959] or delocalized (large polarons) [Fröhlich et al., 1950]. The formation of polarons was observed in many different materials, for example, small polarons were detected in hematite (Fe_2O_3) by Zhou et al. [2019].

Hematite is a promising material for photoelectrochemical water splitting, the process in which water is split into hydrogen and oxygen by sunlight [Sivula et al., 2011, Tamirat et al., 2016]. When a photon of sunlight hits the hematite, an electron-hole pair is created. These charge carriers provide the necessary charge for the water splitting reaction. The main obstacle impeding wider application is that the experimentally achievable efficiency is significantly lower than the theoretically possible one. The limiting factor is the charge carrier mobility. In the case of hematite, the carriers are small polarons. It was observed that doping by titanium [Kronawitter et al., 2014] or nickel [Li et al., 2012], i.e. substitution of one iron atom with titanium or nickel, increases the mobility of electron or hole polarons, respectively.

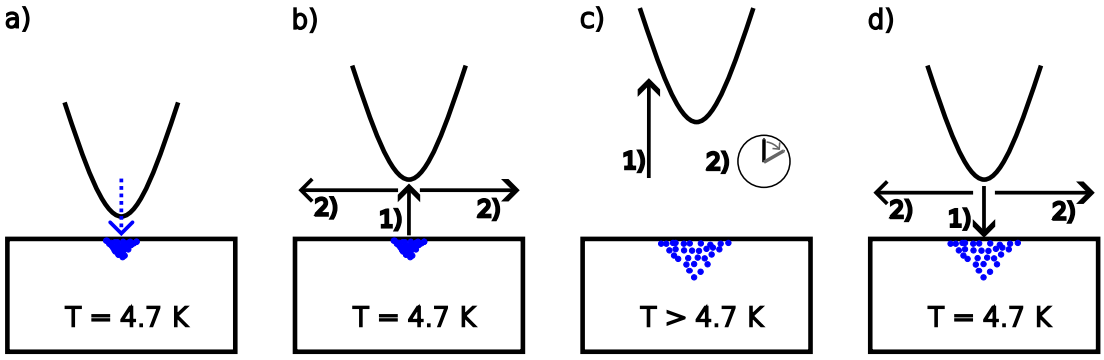

Figure 3.1: The schematic of the polarons injection (blue circles). a) The tip approaches near the hematite surface. b) The tip is slightly retracted 1) to measure the outside potential 2). c) The tip is retracted far away from the sample 1) to reduce its influence on the polaron mobility and the sample is annealed for about 10 minutes 2). d) The sample is cooled back to 4.7 K and the tip approaches the sample 1) to measure the outside potential 2). Then, the steps c) and d) are repeated until the set of temperatures is measured.

In the experiment made in Martin Setvin's group, a diffusion of polarons in hematite was studied. For the study, about 300 polarons from the tip of a qPlus AFM sensor [Giessibl, 2019] were injected into the sample at 4.7 K (Fig. 3.1 a)). After the injection, the tip was retracted and the local contact potential difference (CPD) was measured at a constant distance above the injection point using Kelvin probe force microscopy (KPFM) (Fig. 3.1 b)) [Nonnenmacher et al., 1991, Zerweck et al., 2005]. The tip was then retracted further away from the sample to reduce its influence on the polarons. The sample with the injected polarons was kept

at low temperature (4.7 K) for a long period of time to ensure that they were not mobile under these conditions. Subsequently, the tip was again put near the sample and the potential map was measured. The tip was then retracted and the sample was annealed for ten minutes at a higher temperature (Fig. 3.1 c)). After the annealing was completed, the sample was cooled again to 4.7 K and the outside potential was measured (Fig. 3.1 d)). The procedure described above was repeated for a set of temperatures. For clarity, a 1D cut including the maximum of each potential map was plotted (Fig. 3.2).

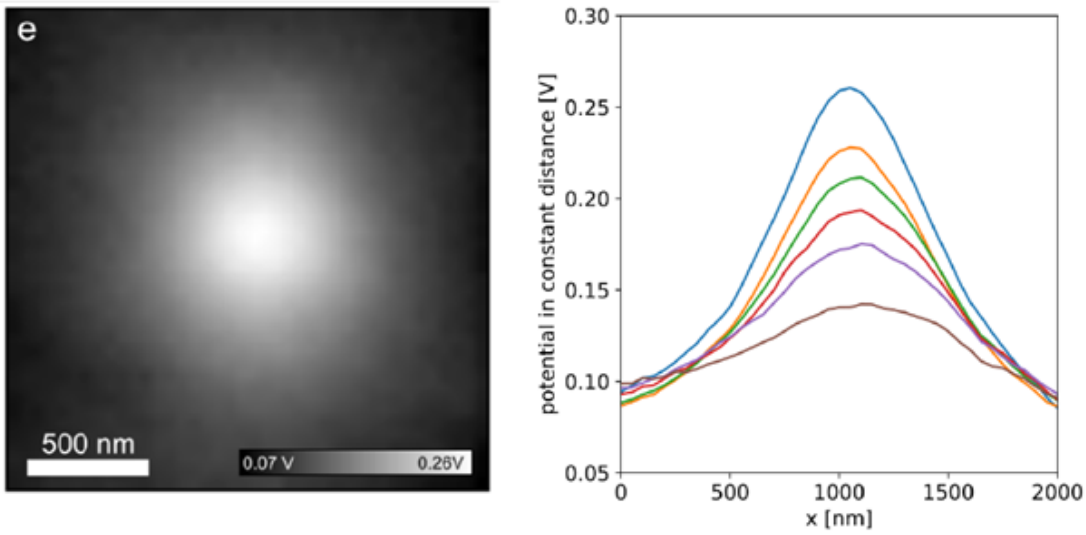

Figure 3.2: Example of the measured potential map and the set of 1D cuts through the maps. The potentials were measured along the diagonal line.

To study the dependence of polaron mobility on doping, the experiment was repeated with the hematite sample doped with various amounts of titanium.

3.1 Model of polaronic diffusion

The experimental data against which the model results are compared were presented in the previous section. In this section, we present the kMC model to simulate the polaronic diffusion. In all the simulations, the annealing and cooling cycle (presented in Fig. 3.1) are the same as in the experiment. The kMC model is a 3D cubic lattice diffusion model. During each time-step, one polaron is either injected or jumps to a neighboring cell. A diffusion barrier E_D is present between every two cells (see Fig. 3.3 b)). To calculate the rate of possible jumps of polaron i, it is necessary to compute the electrostatic potential $V_{in}(\mathbf{r}_{in})$ around polaron n acting on polaron i

$$V_{in}(\mathbf{r}_{in}) = \frac{q_n}{4\pi\varepsilon|\mathbf{r}_{in}|}, \tag{3.1}$$

q_n is the charge of polaron n, $|\mathbf{r}_{in}|$ is the distance between the polaron i and the polaron n and ε is the permittivity of the material. Here and in the following we assume that $i \neq n$.

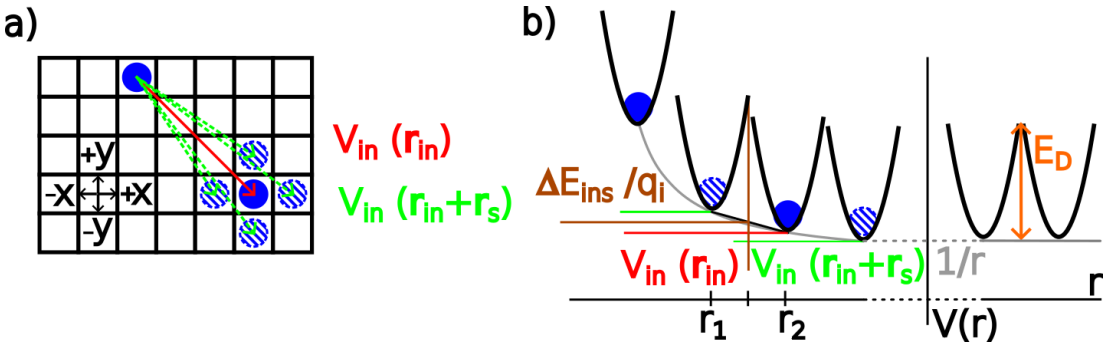

Figure 3.3: a) A 2D sketch to illustrate how $V_{in}(\mathbf{r}_{in}+\mathbf{r}_s)$ is determined. First, $V_{in}(\mathbf{r}_{in})$ (red line) is enumerated for original configuration of polarons i and n and $V_{in}(\mathbf{r}_{in}+\mathbf{r}_s)$ (green dashed lines) is calculated for the polaron i moved to the neighboring cell (dashed circles). b) An explanation of the one half factor in the Eq. 3.2 for ΔE_{ins}. The diffusion barrier E_D is assumed to be present at the centre between two cells. $V_{in}(\mathbf{r}_{in})$ and $V_{in}(\mathbf{r}_{in}+\mathbf{r}_s)$ are calculated in original (filled circle) and neighboring (dashed circles) positions, respectively. The 1/r dependence (gray profile) in the potential equation (Eq. 3.1) is linearly interpolated (black line) between r_1 and r_2 (the neighboring and given positions, respectively). At the center between these two points, the diffusion barrier is modified by potential $\frac{1}{2}[V_{in}(\mathbf{r}_{in}+\mathbf{r}_s)-V_{in}(\mathbf{r}_{in})]$.

To determine the rate of a jump to the neighboring cell by vector $\mathbf{r}_s$ (change of x or y or z component of the vector $\mathbf{r}_{in}$ by $\pm$ unit cell size), the difference of the electrostatic potential in the neighboring cell and original cell multiplied by q_i, ΔE_{ins} needs to be determined (Fig. 3.3 b)). Hence, the electrostatic potential has to be enumerated in the original positions of polarons $\mathbf{r}_{in}$ and in the neighboring cells $\mathbf{r}_{in}+\mathbf{r}_s$

$$\Delta E_{ins} = \frac{q_i}{2}[V_{in}(\mathbf{r}_{in}+\mathbf{r}_s)-V_{in}(\mathbf{r}_{in})]. \tag{3.2}$$

The one half factor in Eq. 3.2 is based on the assumption that the distance between two neighboring cells is small, so the potential can be linearized between them. The potential difference in the central point between two cells is $\frac{1}{2}[V_{in}(\mathbf{r}_{in}+\mathbf{r}_s)-V_{in}(\mathbf{r}_{in})]$ (see Fig. 3.3 b)). Then, the rate of jump in the direction $\mathbf{r}_s$ of polaron i can be determined as

$$R_{is} = R_0 \exp\left(-\frac{E_D+\Delta E_{is}}{k_b T}\right), \tag{3.3}$$

where R_0 is the prefactor, $\Delta E_{is} = \sum_{n=1}^{n\leq N} \Delta E_{ins}$, N is the number of polarons, k_b the Boltzmann constant and T the sample temperature. To obtain the total rate R during each time-step, the partial rates R_{is} has to be summed

$$R = \sum_{i=1}^{i\leq N} \sum_{\mathbf{r}_s\in\{\pm x,\pm y,\pm z\}} R_{is}, \tag{3.4}$$

where the second summation is performed over six different cells in the 3D cubic lattice neighboring the current cell containing polaron i.

After every polaron movement, all the corresponding potentials $V_{in}(\mathbf{r}_{in})$, barrier changes ΔE_{ins}, and rates R_{is}, and R have to be recalculated. The presented

model was designed to efficiently calculate these updates and thus be able to simulate domains with hundreds of thousands of interacting positive and negative charges. Information about the implementation is in Section 3.3.

3.2 Simulation results

In this section, we present the results of our polaron simulations. First, we focus on polaronic diffusion in titanium-doped hematite. Using these data, we describe the behavior of the model. Furthermore, we use the model to simulate different phenomena observed during experiments with polarons.

The measurements were made mostly by Jesus Redondo at TU Wien and Dominik Wrana at Charles University. They used KPFM to study the movement of about 300 polarons inside hematite. Four different hematite samples with different titanium dopancies were measured - 0 % (Fig. 3.4 a)), 0.03 % (Fig. 3.4 b)), 0.7 % (Fig. 3.4 c)), and 3 % (Fig. 3.4 d)), i.e., x % of iron atoms in the hematite was substituted by titanium. Comparing the profiles for temperatures 11 K in Figs. 3.4 a) and b) and 10 K in Figs. 3.4 c) and d), we see that increasing dopancy leads to broader profiles. This indicates that the injected polarons diffuse further away from the injection point in approximately the same time period. Thus, the diffusion (speed) and polaron mobility increases with increasing titanium dopancy. In the case of the undoped sample, the measurements were not fully aligned due to the use of an asymmetric AFM tip.

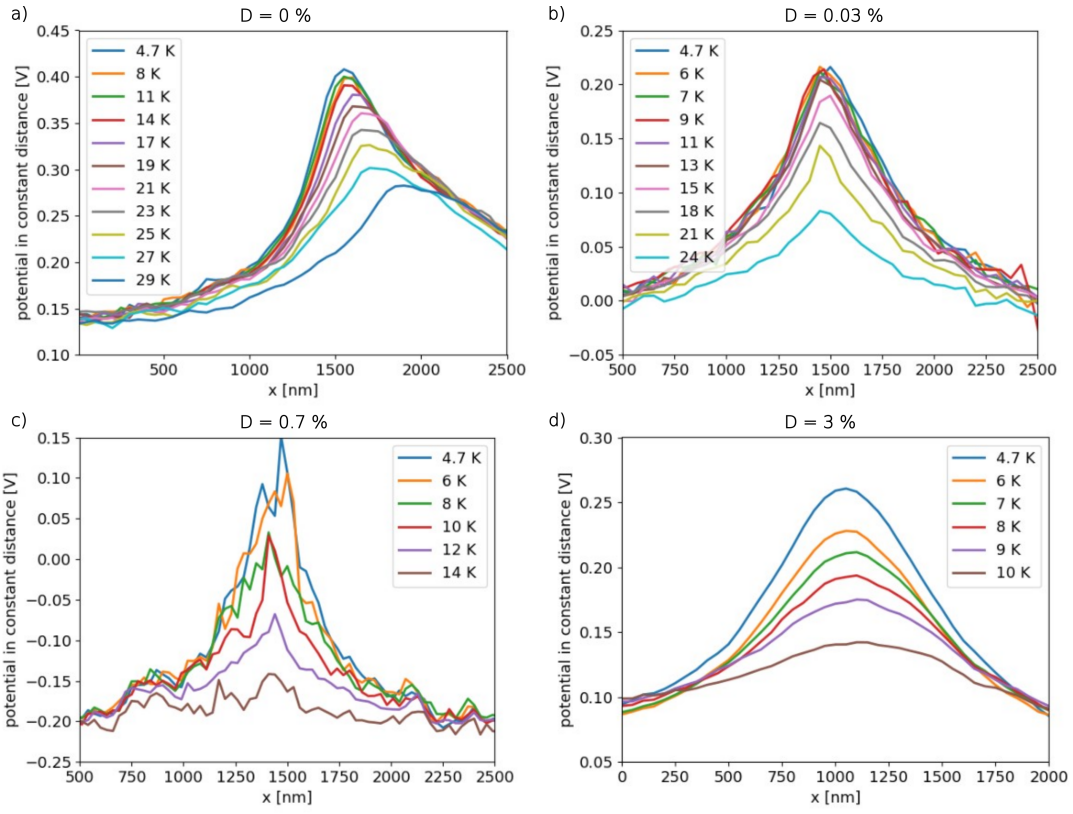

Figure 3.4: The measured CPDs for dopancies a) 0 %, b) 0.03 %, c) 0.7 % and d) 3 %.

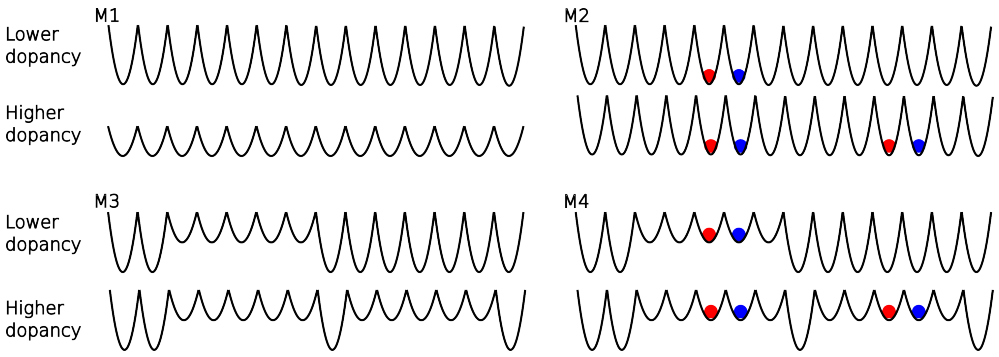

Figure 3.5: Illustration of the differences between the four models (M1 - M4). For each of them, the top row shows the realization of the model with the lower dopancy, and the bottom row corresponds to the higher dopancy. The red and blue circles denote dopant's positive and negative charge, respectively.

The kMC model presented in the previous section was used to describe the polaronic diffusion in the titanium-doped hematite and to understand the mechanism by which doping affects diffusion. The studied dopancies were the same as in the experiment, i.e., 0 %, 0.03 %, 0.7 % and 3 %. Four variants of the model were tested. Each of them simulated the presence of dopants and the diffusion barrier differently. Figure 3.5 illustrates the four models:

Model 1 (M1): The diffusion barrier E_D is constant in the whole domain. Increased dopancy decreases the barrier, i.e. $E_{D;0\%} > E_{D;0.03\%} > E_{D;0.7\%} > E_{D;3\%}$.

Model 2 (M2): Dopants influence the injected polaron by electrostatic potential in their vicinity. Using ab-initio simulations, it was found that electrons are located in the vicinity of titanium [Liao et al., 2011]. Hence, dopants are modeled by a pair of mobile negative charge (electron) and static positive charge (titanium). At the start of the simulation, these two charges are in two neighboring cells. The number of pairs is determined by dopancy. The cells in which the positive charges are located are chosen randomly. We assume that in their vicinity, the difference in the exact location of the positive and negative charges should affect the polaron mobility, while at larger distances both added charges should cancel each out. The diffusion barrier $E_D = E_{D;0\%}$ is constant in the whole domain for all the dopancies. This value is chosen to test whether the presence of the pairs are sufficient to increase the mobility of the injected polarons.

Model 3 (M3): Dopants locally reduce the diffusion barrier. Dopants are modeled without putting additional charges into the domain. Random cells are chosen where the dopant is assumed to be present. In a sphere of radius a around the chosen cells, the diffusion barrier is set as for the highest dopancy in M1, i.e., $E_D = E_{D;3\%}$. Everywhere else, the diffusion barrier is set as $E_D = E_{D;0\%}$. The electrostatic interaction with dopants is neglected.

Model 4 (M4): The dopants are modeled by both the charge pair and the decreased barrier in the sphere around the positive charge. The barrier configuration is the same as in M3.

3.2.1 Model 1: Barrier constant in the whole domain

In this section, we describe the basic model of the titanium dopping influence. The diffusion barriers between any two cells (E_D in Eq. 3.3) are constant. The barriers were estimated from the measured data: From the CPD measurements, we determined the temperature T_0 at which each polaron jumps on average about once per minute. Setting R_i in Eq. 1.2 to 1/60 and $T = T_0$ gives the energy barrier dependent on the prefactor R_0. Two different prefactors were used, $R_0 = 10^6$ s^{-1} and $R_0 = 10^{11}$ s^{-1}. The value $R_0 = 10^{11}$ s^{-1} was chosen as it is the phonon frequency. However, as it is shown below, the values $R_0 = 10^6$ s^{-1} leads to better results. The corresponding barriers E_D are presented in Table 3.1.

Dopancy [%]	0	0.03	0.7	3
T_0 [K]	29	21	10	7
E_D for $R_0 = 10^{11}$ s^{-1} [meV]	74	53	25	18
E_D for $R_0 = 10^6$ s^{-1} [meV]	45	32	16	11

Table 3.1: The diffusion barriers E_D for all the measured titanium dopancies and both studied prefactors.

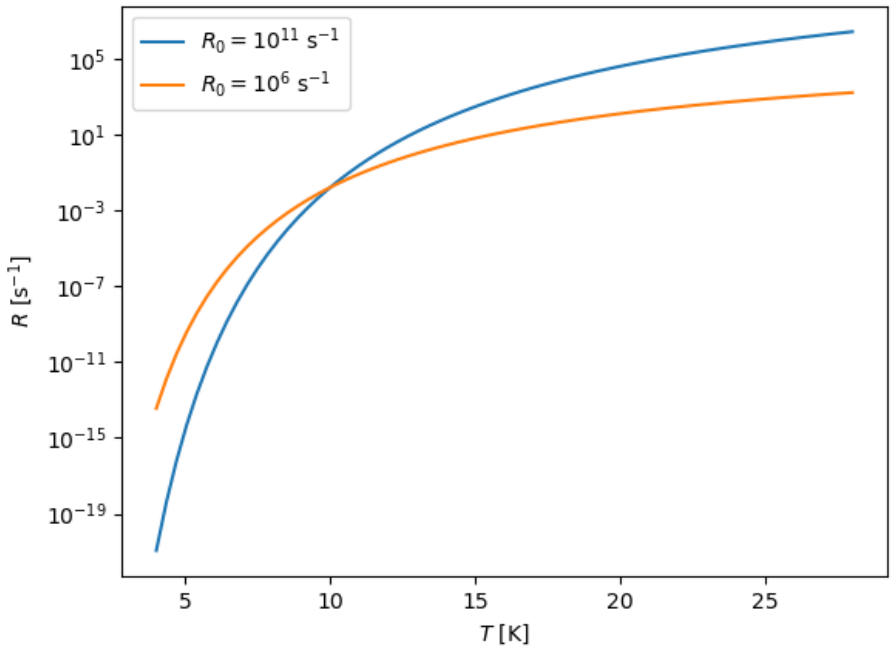

Figure 3.6: The diffusion rate R as a function of the temperature T for $R_0 = 10^6$ s^{-1} (orange) and $R_0 = 10^{11}$ s^{-1} (blue). E_D is taken from Table 3.1 for 0.7 % dopancy.

Figure 3.6 shows the rate R of jump over the barrier as a function of temperature T for both prefactors. Both profiles intersect at $T = 10$ K $= T_0$. For temperatures lower than T_0, the rates are higher for the lower prefactor, and vice versa. Next, we present two sets of results, one for each prefactor, and discuss the influence of the prefactor in more detail.

Figure 3.7 shows an example of the polaron cloud after three annealing cycles. The polaron positions are captured at the ends of three annealing cycles (4.7 K

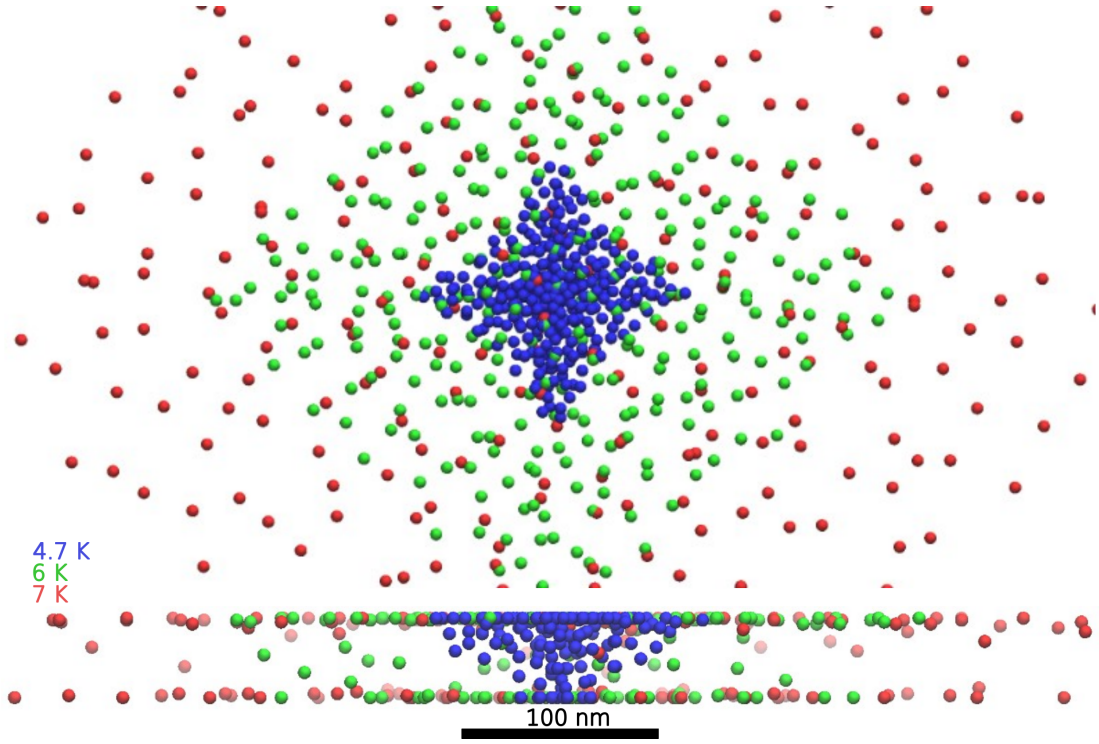

Figure 3.7: Top and side view of an example of the polaronic diffusion at the end of three different annealing cycles - 4.7 K (blue), 6 K (green), and 7 K (red).

- blue, 6 K - green, 7 K - red) right before the next annealing starts. During the injection and the first annealing cycle (4.7 K), the polaron mobility is very low. They form a pyramid-like shape with the majority of polarons along the x and y axes. After the second annealing, the cloud expands due to repulsive electrostatic interaction between polarons and increased rate of polaron hopping. The polaron hopping rate in the absence of electrostatic interaction is inversely proportional to temperature. In the side view, there is a notable separation, with polarons present predominantly on the top or bottom side. The separation is even more pronounced for the highest temperature. It forms because once polarons leave the top side, they are repulsed by all the polarons remaining there until they diffuse to the bottom side. If there were more polarons on the bottom side, the effect would be the same with only the sides swapped. At the highest temperature, the electrostatic repulsion is strong enough compared to the diffusion barrier that the pyramid-like compact structure in the center is no longer present. All the polarons are scattered across the shown part of the simulation domain. Even higher temperatures were simulated, but for them polarons hopped far enough from the center that only a few polarons would still be visible in the shown cutout of the domain. If a larger cutout was shown, the important center of the domain would not be clearly visible. Therefore, the results for the remaining simulated temperatures are not shown in the figure.

Figure 3.8 shows the simulation results for each dopancy and $R_0 = 10^6$ s^{-1} and Fig. 3.9 shows the same for $R_0 = 10^{11}$ s^{-1}. In both figures, panels a) to d) are ordered by dopancy from the lowest to the highest. For comparison with the experiment, the actual values of the outside potential are not important. Two characteristics are needed to understand the experiment: the first is the decrease

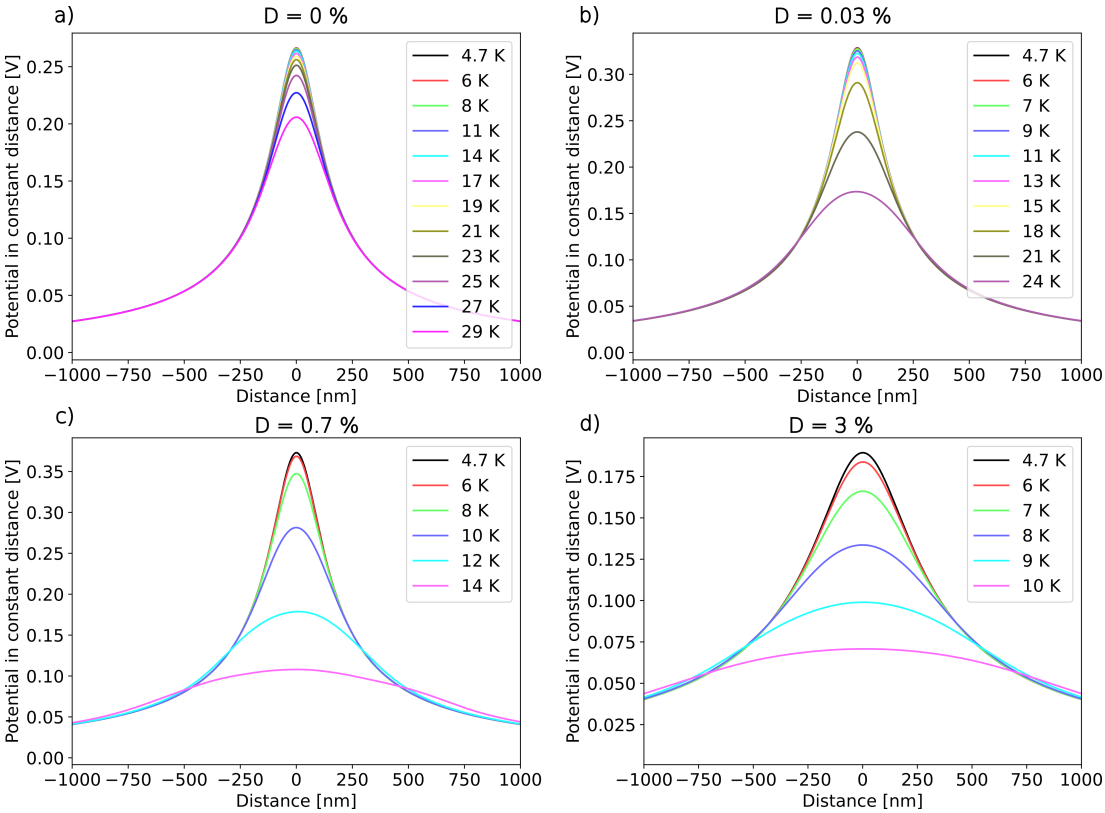

Figure 3.8: The results with the constant diffusion barrier for prefactor $R_0 = 10^6$ s^{-1} and dopancies a) 0 %, b) 0.03 %, c) 0.7 % and d) 3 %.

of maxima, and the second is the potential as a function of distance from the center.

From Fig. 3.6, the influence of the prefactor can be deduced. For temperatures higher than T_0, the diffusion rate, and thus the polaron mobility, is significantly higher for $R_0 = 10^{11}$ s^{-1}. This is evidenced by the larger spacing of each subsequent maxima in Fig. 3.9 a)-d) compared with Fig. 3.8 a)-d). This effect is the most pronounced for the higher two dopancies, where the highest simulated temperature profile is a straight line. Thus, the distribution of polarons in the simulation domain is close to a random distribution. Polarons are no longer predominantly found near the injection point. For temperatures lower than T_0, the spacing between the profiles is slightly bigger for $R_0 = 10^6$ s^{-1}.

Due to the better agreement with the experiment, the lower prefactor is preferred for the simulations of electron polarons. For both prefactors, the decrease and spacing of the maxima behave similarly to the measured data. The difference can be seen at lower temperatures, when the distance between the maxima is larger in the experiment (compare Fig. 3.4 d) with Fig. 3.8 d) and Fig. 3.9 d)). The cause of the issue is that the diffusion rate grows exponentially with temperature. It cannot be sufficiently high at low temperatures to increase the difference between the maxima while not being too high for higher temperatures. Using this model, this issue cannot be avoided unless even smaller prefactor is used. However, the physical interpretation of the $R_0 = 10^6$ s^{-1} and hence of the even smaller prefactor is not clear.

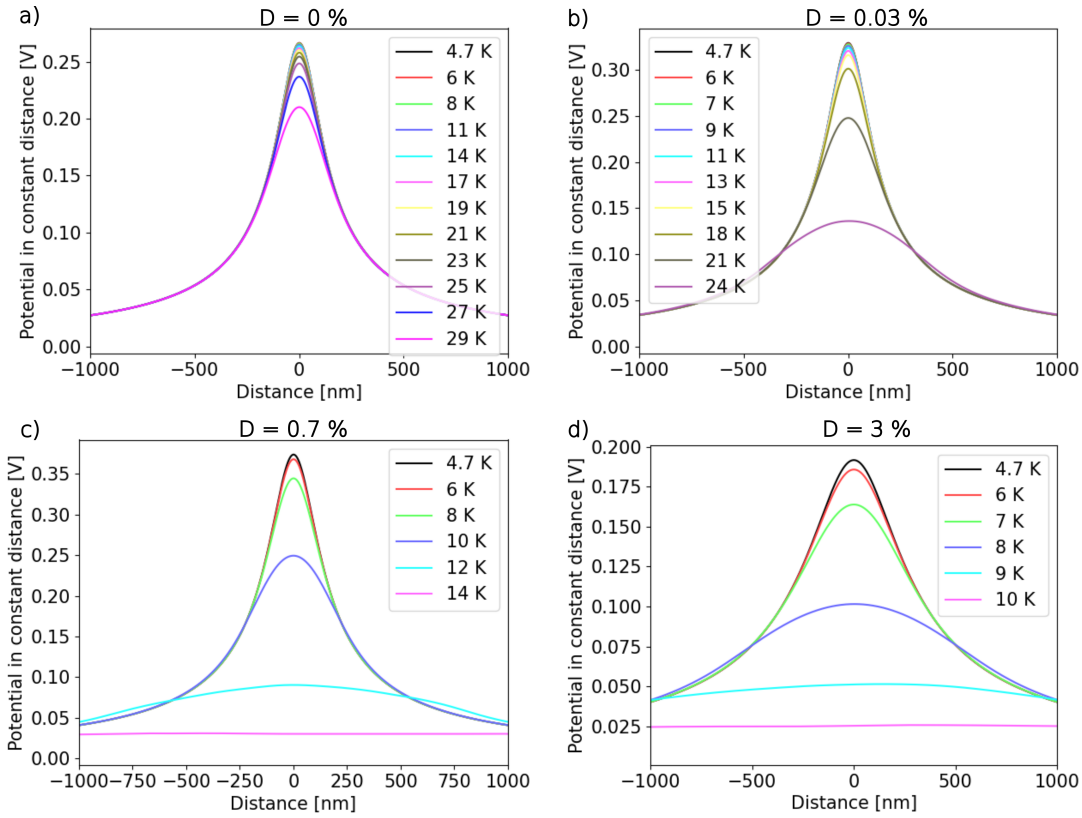

Figure 3.9: The results with the constant diffusion barrier for prefactor $R_0 = 10^{11}$ s^{-1} and dopancies a) 0 %, b) 0.03 %, c) 0.7 % and d) 3 %.

3.2.2 Other models: Dopants influencing the domain only locally

In Section 3.2.1 we introduced the polaronic diffusion model where the diffusion barriers were constant in the whole simulation domain. The results were promising, but the effect of dopants was only considered to be global. To further study whether the global effect can be a sum of local effects, we present three more models (M2 – M4 presented in Section 3.2). Each of them is used to study a different phenomenon which might influence the polaron diffusion: M2 studies the electrostatic potential of dopants, M3 the local effects on the diffusion barrier, and M4 both the electrostatic and local effects of dopants, thus M4 is a combination of M2 and M3. These models are chosen to determine whether the apparent global decrease of barriers may be a combination of local effects.

M2: Dopants influencing the domain by electrostatic interaction

Dopants are simulated as pairs of an immovable positive charge and a movable negatively charged electron polaron to replicate the charge configuration from the ab initio simulations. This configuration is suitable for studying how the electrostatic potential introduced by dopants influences the injected polaron diffusion. The positive charges are randomly distributed in the domain and the negative charges are put in cells neighboring the positive charges. This setup is not feasible for 3 % dopancy and for $R_0 = 10^{11}$ s^{-1} due to the very large number of movable

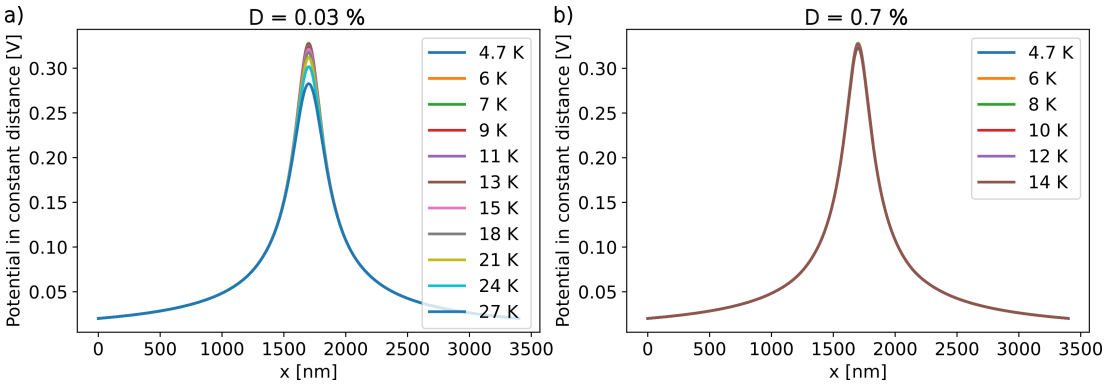

Figure 3.10: Dopants influencing the domain by electrostatic interaction. a), b) simulated outside potential for dopancies 0.03 % and 0.7 %, respectively.

polarons. The barriers between every two cells are set to the value of the undoped sample.

Only the presence of the additional charges may affect the polaronic diffusion compared to M1. Figure 3.10 shows the simulated CPDs for 0.03 % dopancy (panel a)) and 0.7 % dopancy (panel b)). In all the cases, the influence of the additional charges is not sufficient to overcome the diffusion barrier. In addition, polarons are not movable and they get stuck after the injection. This set of simulations proved that the effect of titanium doping goes beyond simple addition of more charges into the system.

M3: Dopants influencing the domain by local decrease of diffusion barriers

Figure 3.11 shows the case in which dopants lower the diffusion barriers (see Fig. 3.5 M3) in their close proximity. If dopants were only decreasing the barriers instead of increasing the minima, the diffusing polarons would be trapped inside the lower barrier areas with only a small probability of leaving them. The barriers are either the same as in the undoped case (far from the nearest dopant) or the same as in the most doped case (close to the nearest dopant). The barriers are chosen based on the assumption that for the highest dopancy, the spheres of the dopant influence overlap completely and there are no barriers which are not close enough to any dopant. Dopants are modeled only by the decreased barrier around the randomly chosen lattice points. The only charges in the model are the injected polarons. This configuration is made to test whether a possible strong local effect is sufficient to explain the observed increase of mobility with dopancy.

Figure 3.11 shows that even though it is possible to find the sphere radii suitable for reproduction of the measured data, these radii are not consistent for the two dopancies shown. For 0.03 % dopancy, the sphere radius is around 7.75 nm. However, it is significantly smaller (around 3.8 nm) for 0.7 % dopancy. Hence, the strong local effect is also not suitable to explain how the dopancy influences the polaron mobility.

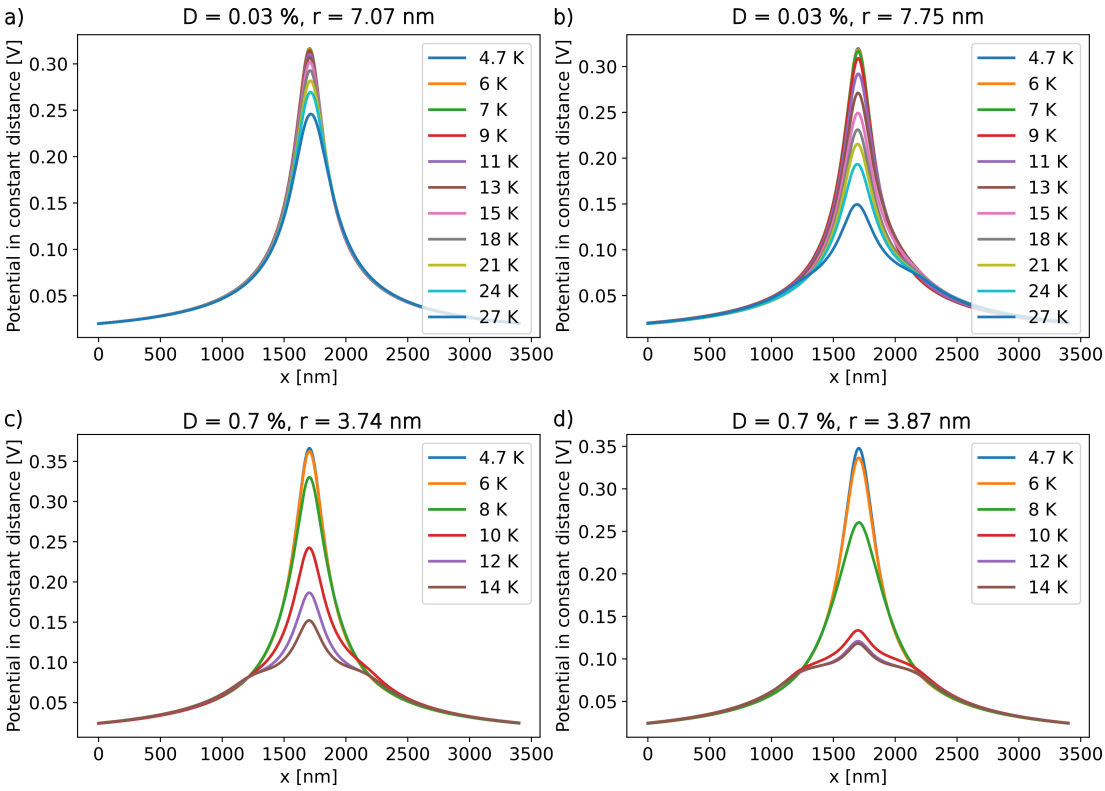

Figure 3.11: Dopants modeled only by the decreased barrier. Two different radii of spheres with decreased barrier are shown for dopancies 0.03 % and 0.7 %.

M4: Dopants influencing the domain by local decrease of diffusion barriers and by electrostatic potential

This model is a combination of the M2 and M3 models. Dopants are modeled by pairs of positive and negative charges and by local barrier decrease. Several simulation runs were made for setups with different radii of the sphere of dopant influence. Figure 3.12 shows an example of result of such simulations. The combination of both effects is not sufficient to fully model the increase of diffusivity with increasing dopancy.

None of the three (M2-M4) models aimed at modelling the local influence of dopants gave results that matched the experiment better than the M1 model. It can be assumed that the influence of the titanium doping is not simply adding more charges and increasing attractive or repulsive electrostatic force or locally decreasing the diffusion barriers. These mechanisms are either not strong enough to significantly influence the polaronic diffusion or they are not consistent for all the dopancies. For further simulations, the M1 model is the preferred choice.

3.2.3 Simulations of hole polarons

In this section, we describe the simulations of small hole polarons in nickel-doped hematite. The main differences between hole and electron polarons lie in the sign of their electric charge and in their mobility. Electron polarons are negatively

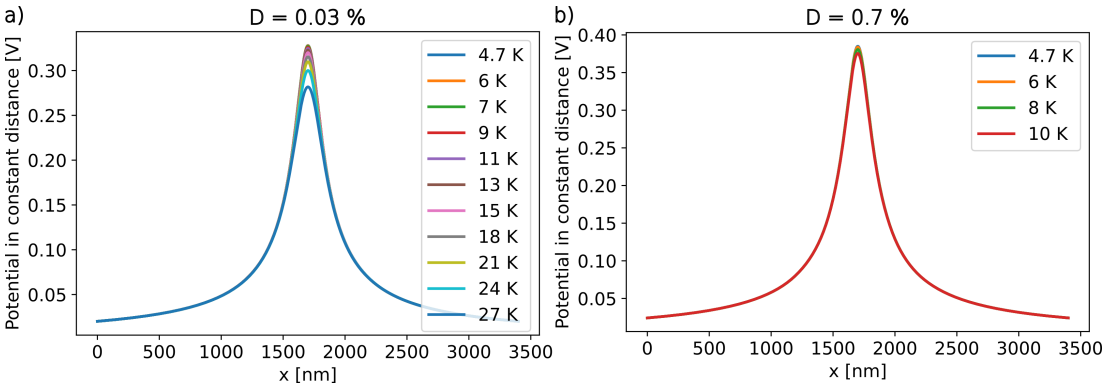

Figure 3.12: Dopants are modeled by both decreased barrier and electrostatic interaction. a) Example for 0.03 % dopancy, the radius of sphere with decreased barrier $r = 2.7$ nm. b) Example for 0.7 % dopancy, the radius of sphere with decreased barrier $r = 2.7$ nm. Note that only temperatures up to 10 K are simulated for 0.7 % dopancy. Simulations for higher temperatures are not possible because all the added pairs of dopants are in the area of decreased barriers.

charged, while hole polarons are positive and have significantly lower mobility. Since the interaction between two polarons depends on the square of their charge (3.2), the M1 model does not need to be modified. The only change is the sign of the potential measured above the sample.

The experimental procedure was mostly the same as for the above described electron polaron measurements. The main distinction was the temperatures at which the CPDs were measured. The difference between the lowest and the highest temperature was significantly larger and fewer measurements were made. To determine the diffusion barrier for hole polaron, we used the relative decrease of CPD the maxima between 77 K and the 91 K. The prefactor and the estimated value of the diffusion barrier were determined from a set of simulations. In the experiment, the ratio of the potential maxima of the two lowest measured temperatures (77 K and 91 K) was approximately 0.75. Using $R_0 = 10^6$ s^{-1}, this ratio could not be reached in the simulation for any diffusion barrier. The lowest ratio achieved was around 0.85 for very low diffusion barriers. For $R_0 = 10^{11}$ s^{-1}, it was possible to find the diffusion barrier $E_D = 200$ meV corresponding to the measured ratio. This is in contrast to the electron polaron simulations where the lower prefactor was the preferable choice.

Figure 3.13 a) shows the measured CPDs of hole polarons. Figure 3.13 b) shows the simulation results for the best-found estimate of the diffusion barrier and prefactor. The main difference between the measured and simulated data is in the profile for the third measured temperature (125 K). In the measured data, there is a very small difference between 91 K and 125 K. We assume that polarons are stuck in trapping centers from which they cannot escape even at the highest temperature. The trapping can be caused, for example, by impurities in the crystal. To quantify the number of traps, we introduced trapping centers into the simulation domain. Polarons are free to move into the trap as if it was a regular cell, but the barrier to jump out is set several orders of magnitude higher (10 eV). The trap positions are chosen randomly. We performed simulations for different concentrations (relative abundances) of traps and the results are shown

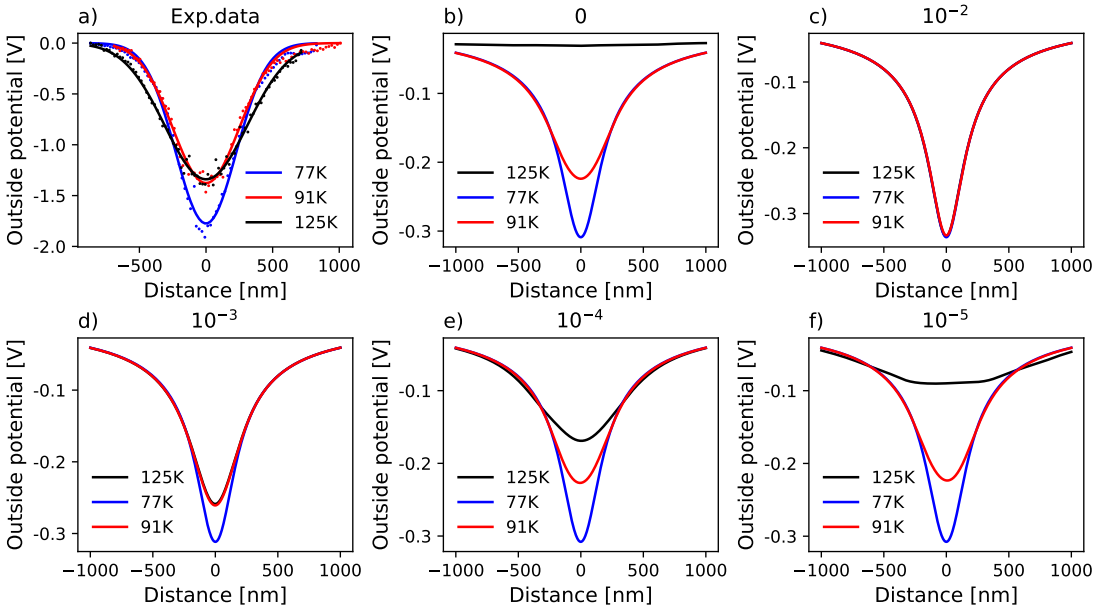

Figure 3.13: a) Measured outside potential for hole polarons. b), c), d), e), f) Simulated outside potential for various concentrations of trapping centers - 0 (no trapping), 10^{-2}, 10^{-3}, 10^{-4}, 10^{-5}, respectively.

in Fig. 3.13 c) - f). The concentration of 10^{-3} (Fig. 3.13 d)) gives the best match between the simulated and measured data. For higher concentration, polarons trapping is too pronounced and all the injected polaron are trapped even at 91 K. On the other hand, smaller concentrations do not sufficiently slow down the polaronic diffusion.

3.2.4 Simulations of the hole polaron injection

The last but not least application of the model presented in the thesis is the study of the hole polaron injection. In all the previous cases, a constant time elapsed between two subsequent injections of polarons. Instead, based on measurements of the times between two polaron injections, we modified the injection to be a new process in the model and to have its own rate.

Figure 3.14 a) and b) shows the measured times elapsed between two individual polaron injections obtained as explained below and the evolution of outside potential during the measurements, respectively. Note that the frequency shift measurements are shown in Fig. 3.14 b) instead of the potential. The frequency shift describes the frequency of the KPFM tip vibrations which is influenced by the potential of polarons. The shape of the frequency shift profile is closely related to the shape of the potential profile.

Figure 3.14 b) shows the frequency shift during polaron injection. Each increase in frequency shift indicates increase in potential of the polaron cloud and hence polaron injection. From the elapsed time between two subsequent frequency shift increases, it is possible to determine the elapsed time between two polaron injections. Figure 3.14 a) shows the measured times between two subsequent polaron injections. At the start of the experiment, the time between injections is very short. As more polarons are injected, the times between injections increase.

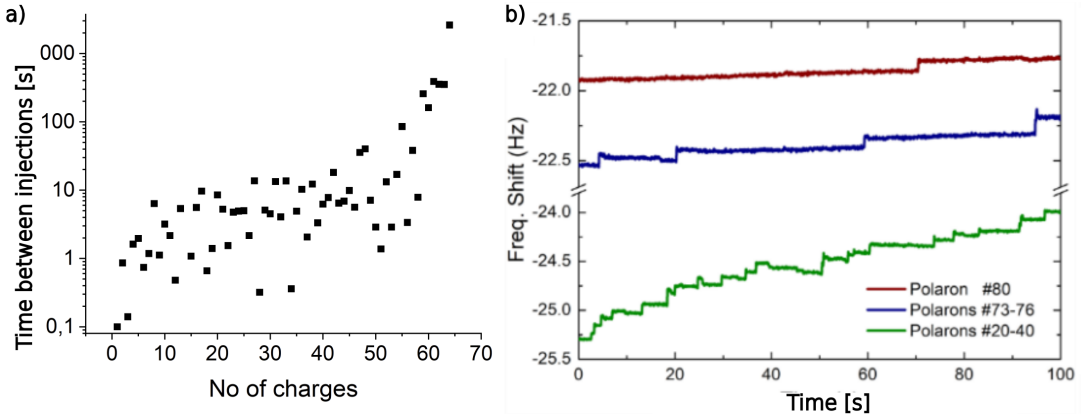

Figure 3.14: a) Measured times between two subsequent polaron injections. b) Snapshots of the measured KPFM frequency shift. The frequency shift is closely related to the outside potential.

This is caused by polarons not hopping from the area under the tip fast enough. Their presence decreases the probability of injection and hence increases the time between two injections. Figure 3.14 b) shows three 100-second snapshots from the experiment, which show the frequency shift measured by KPFM at different stages of the experiment. The increase of frequency shift is generally connected with the polaron injection. The decrease indicates hopping of polaron further away from the tip.

The measured data can be used to modify the simulation of the injection by two different methods. First, the probability of injection per second can be determined from the measured times between injections. Then, the probabilities can be approximated by a polynomial fit, and from this the rates as a function of time can be calculated. This is only a slight modification of the injection and it is set to match the measured data. Second, we can assume that the injected charge with energy E has to tunnel through a potential barrier with height V_0. V_0 is the difference between the tip potential U and the potential acting on the tip from the sample $V_1; V_0 = U - V_1$. The transmission factor T can be calculated as a function of E, V_0 and the distance between the tip and the sample d [Voigtländer, 2015]

$$T = \frac{16E\,(V_0 - E)}{V_0^2} \exp\left(-2d\sqrt{\frac{2m}{\hbar}\,(V_0 - E)}\right), \tag{3.5}$$

where m is the electron mass and $\hbar$ is the reduced Planck constant. The distance of the tip is fixed, $d = 0.5$ nm (Fig. 3.15 a)). For simplicity, the tip can be considered as a conductive sphere with radius $R = 5$ nm (Fig. 3.15 b)). The sphere itself can be modeled by a point charge whose potential at the distance R is equal to U. In this case, it corresponds to approximately 17 positive elementary charges at the distance $d + R = 5.5$ nm (Fig. 3.15 c)).

Using the modified injection, we simulated the time evolution of the outside potential (shown in Fig. 3.16) at the injection point. The results corresponding to the experiment (Fig. 3.14) are presented in Fig. 3.17.

Comparing the times between two subsequent injections (Fig. 3.14 a) and Fig. 3.17 a)) shows that this charge injection model is able to reproduce the measured data very well. Figure 3.17 b) and Fig. 3.14 b) show the outside po-

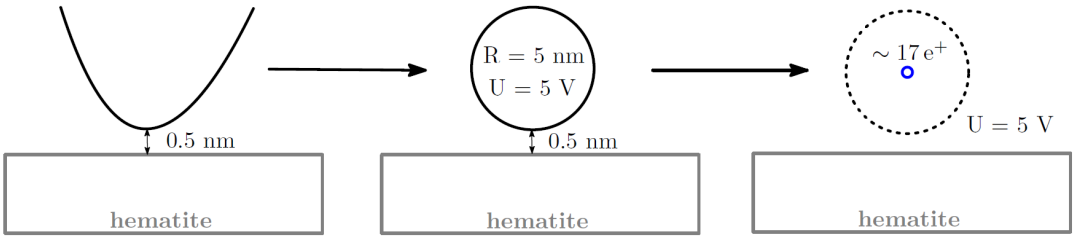

Figure 3.15: The setup of the simulations including the tip. The nearly parabolic tip is approximated by a conductive sphere which is modeled by a point charge at its center.

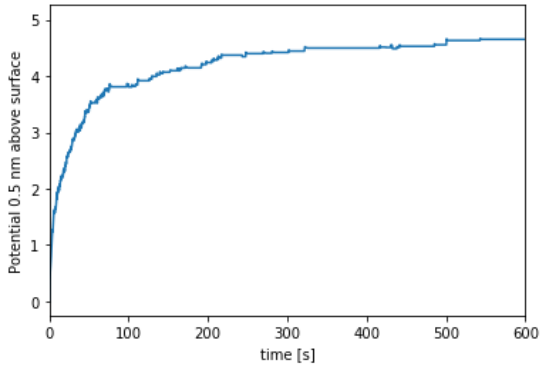

Figure 3.16: The outside potential as a function of time for simulation with the modified polaron injection.

tential evolution for the simulation and experiment, respectively. The simulation data were selected to show the time period corresponding to the experimental data. For the experiment, there are three 100-second snapshots at different stages of the measurement. In all the cases, the simulated outside potential and the measured frequency shift time evolution look similar. For the line labeled "Polaron #80", both data show a singular polaron injection event (increase in potential / frequency shift) followed by a decrease in the measured quantities caused by polaronic diffusion. In the case of the "Polaron #73 – #76" line, both profiles are again very similar. There are several subsequent injections. The most notable is the event at a time of about 240 seconds in the simulated data and 20 seconds in the measured data (note that in the measured data time refers to the time since the start of the highlighted part of the profile; in the simulation it denotes the time elapsed since the start of the simulation). In this case, a clear decrease of both profiles is quickly followed by the polaron injection. In both measured and simulated data, the injection peak is followed by a sharp decrease. This is more evident in the simulated data due to their better time resolution. In the last measured case ("Polaron #20 – #40"), there is a larger difference between the measured and simulated data. However, the general behavior is still similar in both cases. There are many visible injections and jumps of polarons followed by plateaus, suggesting that no events are occurring during these time periods.

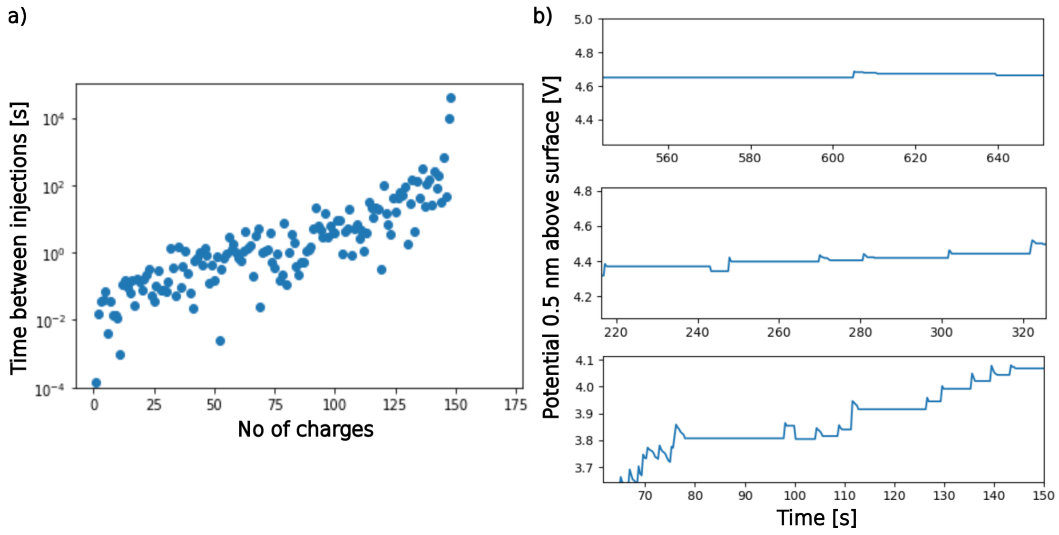

Figure 3.17: a) Simulated times between two subsequent polaron injections. b) Snapshots of the simulated outside potential corresponding to measured data in Fig. 3.14 b).

3.3 Implementation details

Figure 3.18 shows a schematic of the different model versions. The colored squares denote which parts of the numbers stored in memory are calculated at each time-step. The row of squares with the $\sum$ symbol labels the part of the memory which stores the sum of all the squares in the column above. The only exception is Fig. 3.18 c) where all the information is stored in the squares marked with the $\sum$ symbol.

The bottleneck of the model described in Section 3.1 are both the large memory usage and large number of potential calculations. The time complexity of each time-step of the simplest model implementation is of the order of N^2 because all the potentials are recalculated (N^2) and then summed (N) at each time-step. Figure 3.18 a) illustrates the first version of the model. The colored squares are updated during each time-step.

Figure 3.18 b) shows the scheme of significant optimization, i.e., storing the previous values of ΔE_{ins} in a 3D table (dimensions $N \times N \times 6$). During each time-step, only the values associated with the moved polaron are recalculated - the electrostatic potential acting on the moved polaron and the electrostatic potential of the moved polaron acting on all the other polarons. This optimization reduces the time complexity to order of N. If the symmetry of the system $\Delta E_{ins} = \Delta E_{ni(-s)}$ is taken into account, the calculation time can be further halved. This is shown by the identically colored rows and columns in Fig. 3.18 b). The $(-s)$ subscript means that instead of a shift of $\pm x$ or $\pm y$ or $\pm z$ there is a shift of $\mp x$ or $\mp y$ or $\mp z$.

Second optimization is to store the sums R_{is} in memory and at each time-step the previous ΔE_{ins} (which is stored in the 3D matrix) is subtracted from R_{is} and the newly calculated ΔE_{ins} is added. The summation is reduced to two operations for every polaron. The R_{is} of the moved polaron is set to zero and then the calculated values of ΔE_{ins} are added. Figure 3.18 b) also shows

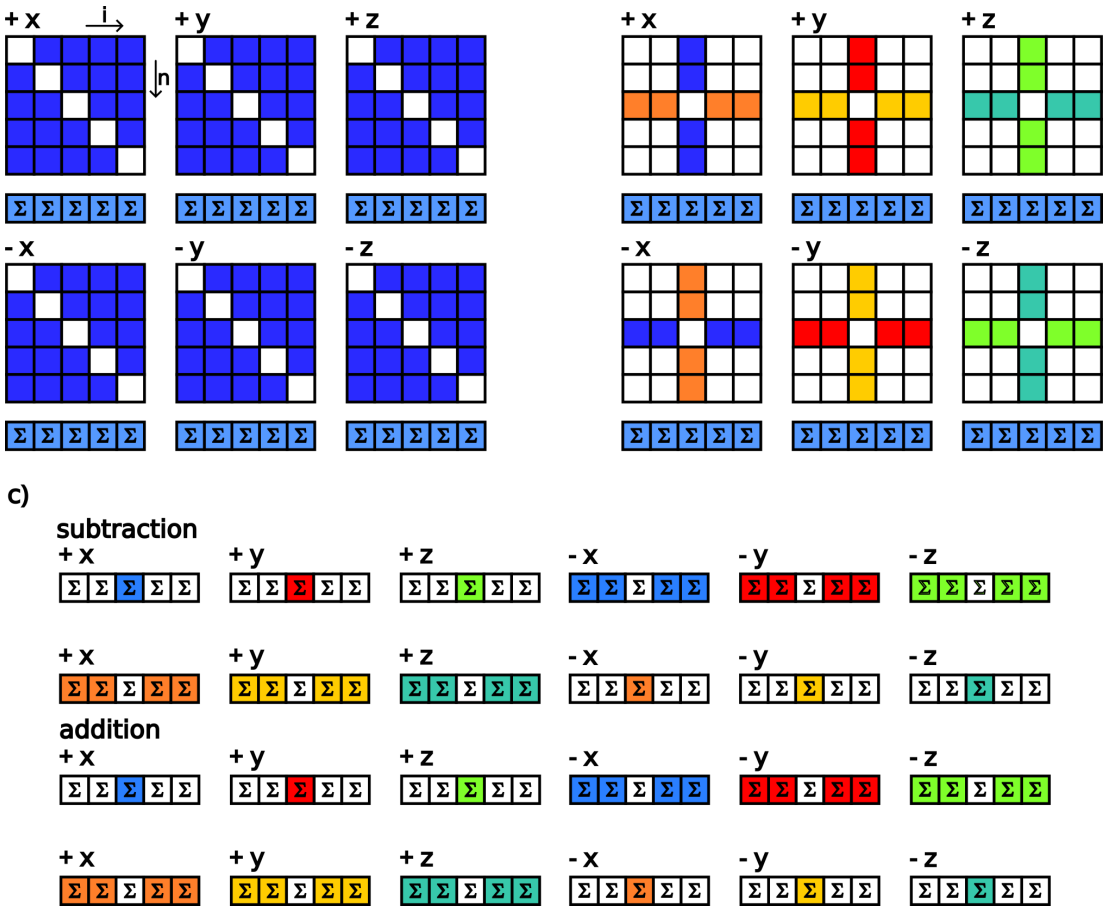

Figure 3.18: The matrix ΔE_{ins} to calculate the rates of hopping of every polaron is shown as cuts in each direction s. Colored squares show which values have to be recalculated every time a polaron moves for: a) the simplest approach where all the values in the table and the column sums are always recalculated. Note, that on the diagonal can be stored non-zero values such as the diffusion barrier. b) The first simplification in calculation of the matrix where only the values corresponding to the moved polarons are calculated. The combination of rows and columns in the same colour show which values are calculated at the same time, e.g., row for $+x$ and column for $-x$. All the column sums has to be recalculated at the end. c) To reduce the computational costs, only the column sums are kept in the memory. The current values for the chosen polaron are first calculated and subtracted and then the new values are added to the sums.

this optimized version of the model in which only subtraction and addition are performed instead of summation of the entire column.

The second optimization gives the most time optimized algorithm. However, for a larger number of interacting polarons, it is not possible to keep all ΔE_{ins} in memory because the size of the table grows as $6N^2$. The memory issue can be eliminated if only partial sums R_{is} are kept (Fig. 3.18 c)). The size of the ΔE_{ins} matrix is N times larger than the size of the R_{is} matrix. To illustrate the difference, consider the M2 model for 0.7 % dopancy . There are about 700 000 moving polarons in the simulation. A memory of about 24 terabytes would be required to store the ΔE_{ins} matrix. In contrast, the R_{is} matrix size is just over 34 megabytes. The disadvantage of this approach is that at each time-step, one

has to not only calculate a new set of ΔE_{ins}, but also recalculate the current set of ΔE_{ins} which is subtracted from R_{is}. In the worst case, if we assume that the summation can be made in much shorter time than the potential calculation, the time necessary for one full simulation is doubled. Even in the worst case, doubling the simulation time is well worth significantly lower memory requirements.

Conclusion

The main aim of the thesis was to apply the kinetic Monte Carlo method on the problems of pulsed-laser deposition growth of thin films and on polaronic diffusion.

We designed and developed a novel model for the simulations of PLD growth. Unlike the widely used models, the new model does not resolve diffusion as a random walk but simulates it by inclusion of the unit gas which is equivalent to the limit of fast diffusion. This model was first validated with data from literature and subsequently used to clarify some of the phenomena observed during PLD growth. There are two major results. First, the inter-layer transport can be considered as a single process even though there are two typical timescales. Second, the decreasing roughness of the resulting film with increasing laser frequency is not an effect of the laser frequency itself. We found that increasing the laser frequency leads to more coarse surfaces. We determined that the increase of the surface and substrate temperature was responsible for the increased smoothness. This effect is especially pronounced for substrates with low thermal conductivity.

Next, we used the model of polaronic diffusion to further understand how the dopancy affects charge transfer in hematite. For this purpose, we made a model which included all the electrostatic interactions of the injected polarons. We studied several approximations of how dopants could influence the charge transfer, namely the diffusion barriers. Even though we implemented three more precise models which introduced dopants into the simulation domain, we found that the most successful model was the simplest one. In it, we model dopants only by decreasing all the diffusion barriers in the whole domain. We were able to determine that any combination of local influences such as the locally decreased barriers is not sufficient to correctly reproduce the experimental data. This leads to understanding that in reality there has to be a process which is responsible for the global barrier reduction when the titanium doping is present. The model was also used to study hole polarons in nickel-doped hematite. The main discrepancy between the electron and hole polaron simulations was in the used prefactor. For electron polarons, the most suitable one was $10^6\,\mathrm{s}^{-1}$ while for hole polarons it was $10^{11}\,\mathrm{s}^{-1}$. This hints that the diffusion process of each polaron type is different. However, this question cannot be fully answered using the kMC model. We also simulated the process of the injection of the hole polarons. In this case, the only additional assumption we made was that holes tunnel through the energy barrier between the AFM tip and the hematite surface. The tunneling rate is only a function of the local potential. Even with this general setup, we were able to reproduce the measurements made during the injection process, including changes of the measured outside potential at one location above the surface.

Bibliography

B. J. Alder and T. E. Wainwright. Studies in molecular dynamics. I. general method. *J. Chem. Phys.*, 31(2):459–466, 1959.

M. Andersen, C. Panosetti, and K. Reuter. A practical guide to surface kinetic Monte Carlo simulations. *Front. Chem.*, 7, 2019.

A.-L. Barabási and H. E. Stanley. *Fractal Concepts in Surface Growth*. Cambridge University Press, 1995. ISBN 9780511599798.

S. Bauer, A. Rodrigues, L. Horák, X. Jin, R. Schneider, T. Baumbach, and V. Holý. Structure quality of $LuFeO_3$ epitaxial layers grown by pulsed-laser deposition on sapphire/Pt. *Materials*, 13(1), 2020.

J. R. Beeler. Displacement spikes in cubic metals. i. α-iron, copper, and tungsten. *Phys. Rev.*, 150:470–487, 1966.

A. B. Bortz, M. H. Kalos, and J. L. Lebowitz. A new algorithm for Monte Carlo simulation of Ising spin systems. *J. Comput. Phys.*, 17(1):10 – 18, 1975.

P. Brandimarte. *Handbook in Monte Carlo simulation: applications in financial engineering, risk management, and economics*. Wiley handbooks in financial engineering and econometrics. Wiley, Hoboken, 2014. ISBN 9780470531112.

D. B. Chrisey and Gr. K. et. al. Hubler. Pulsed laser deposition of thin films. 1994.

H. M Christen and G. Eres. Recent advances in pulsed-laser deposition of complex oxides. *J. Phys.: Condens. Matter*, 20(26):264005, 2008.

C. Domain, C. S. Becquart, and L. Malerba. Simulation of radiation damage in Fe alloys: an object kinetic Monte Carlo approach. *J. Nucl. Mater.*, 335(1): 121–145, 2004.

C. Ederer and C. J. Fennie. Electric-field switchable magnetization via the Bzyaloshinskii–Moriya interaction: $FeTiO_3$ versus $BiFeO_3$. *J. Phys.: Condens. Matter*, 20(43):434219, 2008.

G. Ehrlich and F. G. Hudda. Atomic view of surface self-diffusion: tungsten on tungsten. *J. Chem. Phys.*, 44(3):1039–1049, 1966.

G. Eres, J. Z. Tischler, C. M. Rouleau, P. Zschack, H. M. Christen, and B. C. Larson. Quantitative determination of energy enhanced interlayer transport in pulsed laser deposition of $SrTiO_3$. *Phys. Rev. B*, 84:195467, 2011.

J. D. Ferguson, G. Arikan, D. S. Dale, A. R. Woll, and J. D. Brock. Measurements of surface diffusivity and coarsening during pulsed laser deposition. *Phys. Rev. Lett.*, 103(25):256103, 2009.

C. Franchini, M. Reticcioli, M. Setvín, and U. Diebold. Polarons in materials. *Nat. Rev. Mater.*, 6(7):560–586, 2021.

H. Fröhlich, H. Pelzer, and S. Zienau. XX. Properties of slow electrons in polar materials. *Lond. Edinb. Phil. Mag*, 41(314):221–242, 1950.

V. Gabriel, P. Kocán, and V. Holý. Effective algorithm for simulations of layer-by-layer growth during pulsed-laser deposition. *Phys. Rev. E*, 102:063305, 2020.

V. Gabriel, P. Kocán, S. Bauer, B. Nergis, A. Rodrigues, L. Horák, X. Jin, R. Schneider, T. Baumbach, and V. Holý. Effect of pulse laser frequency on PLD growth of $LuFeO_3$ explained by kinetic simulations of in-situ diffracted intensities. *Sci. Rep.*, 12(1):5647, 2022a.

V. Gabriel, P. Kocán, and V. Holý. Growth-rate model of epitaxial layer-by-layer growth by pulsed-laser deposition. *Phys. Rev. E*, 106:035302, 2022b.

C. J. Geyer. Practical markov chain Monte Carlo. *Stat. Sci.*, 7(4):473–483, 1992.

F. J. Giessibl. The qPlus sensor, a powerful core for the atomic force microscope. *Rev. Sci. Instrum.*, 90(1):011101, 2019.

N. A. Hill. Why are there so few magnetic ferroelectrics? *J. Phys. Chem. B*, 104 (29):6694–6709, 2000.

T. Holstein. Studies of polaron motion: Part II. The "small" polaron. *Ann. Phys.*, 8(3):343–389, 1959.

J.-M. Hu, L.-Q. Chen, and C.-W. Nan. Multiferroic heterostructures integrating ferroelectric and magnetic materials. *Adv. Mater.*, 28(1):15–39, 2016.

L. Huang. Kinetic Monte Carlo simulations for the submonolayer growth of homoepitaxial $SrTiO_3$ thin films. *Micro Nano Lett.*, 13(10):1497–1500, 2018.

D.A. King and D.P. Woodruff. *Growth and Properties of Ultrathin Epitaxial Layers*. ISSN. Elsevier Science, 1997. ISBN 978-0-08-053267-7.

D. P. Kroese, T. Brereton, T. Taimre, and Z. I. Botev. Why the Monte Carlo method is so important today. *WIREs Comput. Stat.*, 6(6):386–392, 2014.

C. X. Kronawitter, I. Zegkinoglou, S.-H. Shen, P. Liao, I. S. Cho, O. Zandi, Y.-S. Liu, K. Lashgari, G. Westin, J.-H. Guo, F. J. Himpsel, E. A. Carter, X. L. Zheng, T. W. Hamann, B. E. Koel, S. S. Mao, and L. Vayssieres. Titanium incorporation into hematite photoelectrodes: theoretical considerations and experimental observations. *Energy Environ. Sci.*, 7(1):31–3121, 2014.

A. Lecchini Visintini, W. Glover, J. Lygeros, and J. Maciejowski. Monte Carlo optimization for conflict resolution in air traffic control. *IEEE Trans. Intell. Transp. Syst.*, 7(4):470–482, 2006.

J. Li, F. Meng, S. Suri, We. Ding, F. Huang, and N. Wu. Photoelectrochemical performance enhanced by a nickel oxide–hematite p–n junction photoanode. *ChemComm*, 48(66):8213–8215, 2012.

Y. Li, C. J. Lu, J. Su, Y. C. Zhang, C. Zhang, S. F. Zhao, X. X. Wang, D. J. Zhang, and H. M. Yin. Room-temperature multiferroic $Bi_4YFeTi_3O_{15}$ thin films of four-layered perovskite. *J. Alloys Compd.*, 687:707–711, 2016.

P. Liao, M. C. Toroker, and E. A. Carter. Electron transport in pure and doped hematite. *Nano lett.*, 11(4):1775–1781, 2011.

Y. Maeno, H. Hashimoto, K. Yoshida, S. Nishizaki, T. Fujita, J. G. Bednorz, and F. Lichtenberg. Superconductivity in a layered perovskite without copper. *Nature*, 372(6506):532–534, 1994.

P. A. Maksym. Fast Monte Carlo simulation of MBE growth. *Semicond. Sci. Technol.*, 3(6):594–596, 1988.

B. F. J. Manly. *Randomization, bootstrap and Monte Carlo methods in biology.* Texts in statistical science. CRC Press, Taylor & Francis Group, Boca Raton, Florida, 2021. ISBN 978-0-367-51287-3.

N. Metropolis, A. W. Rosenbluth, M. N. Rosenbluth, A. H. Teller, and E. Teller. Equation of state calculations by fast computing machines. *J. Chem. Phys.*, 21(6):1087–1092, 1953.

M. Nonnenmacher, M. P. O'Boyle, and H. K. Wickramasinghe. Kelvin probe force microscopy. *Appl. Phys. Lett.*, 58(25):2921–2923, 1991.

K. Ohno. *Computational materials science: from Ab initio to Monte Carlo methods.* Springer series in solid-state sciences ; 129. Springer, Berlin, 1999. ISBN 3-540-63961-6.

N.-G. Park. Perovskite solar cells: an emerging photovoltaic technology. *Mater. Today*, 18(2):65–72, 2015.

M. R. Rashidian Vaziri, F. Hajiesmaeilbaigi, and M. H. Maleki. Monte Carlo simulation of the subsurface growth mode during pulsed laser deposition. *J. Appl. Phys.*, 110(4):043304, 2011.

J. Redondo, M. Reticcioli, V. Gabriel, D. Wrana, F. Ellinger, M. Riva, G. Franceschi, E. Rheinfrank, I. Sokolovic, Z. Jakub, F. Kraushofer, A. Alexander, L. L. Patera, J. Repp, M. Schmid, U. Diebold, G. S. Parkinson, C. Franchini, P. Kocán, and M. Setvín. Real-space investigation of polarons in hematite Fe_2O_3. *arXiv preprint arXiv:2303.17945*, 2023.

R. L. Schwoebel and E. J. Shipsey. Step motion on crystal surfaces. *J. Appl. Phys.*, 37(10):3682–3686, 1966.

K. Sivula, F. Le Formal, and M. Grätzel. Solar water splitting: Progress using hematite (α-Fe_2O_3) photoelectrodes. *ChemSusChem*, 4(4):432–449, 2011.

N. K. Tailor, M. Abdi-Jalebi, V. Gupta, H. Hu, M. I. Dar, G. Li, and S. Satapathi. Recent progress in morphology optimization in perovskite solar cell. *J. Mater. Chem.A*, 8(41):21356–21386, 2020.

A. G. Tamirat, J. Rick, A. A. Dubale, W.-N. Su, and B.-J. Hwang. Using hematite for photoelectrochemical water splitting: a review of current progress and challenges. *Nanoscale Horiz.*, 1(4):243–267, 2016.

J. A. Venables. Rate equation approaches to thin film nucleation kinetics. *Philos. Mag.*, 27(3):697–738, 1973.

E. Vlieg, A. W. D. van der Gon, J. F. Van der Veen, J. E. MacDonald, and C. Norris. Surface X-ray scattering during crystal growth: Ge on Ge (111). *Phys. Rev. Lett.*, 61(19):2241, 1988.

B. Voigtländer. *Scanning probe microscopy: atomic force microscopy and scanning tunneling microscopy*. NanoScience and Technology. Springer, New York, 2015. ISBN 978-3-662-45239-4.

A. F. Voter. Introduction to the kinetic Monte Carlo method. In K. E. Sickafus, E. A. Kotomin, and B. P. Uberuaga, editors, *Radiation Effects in Solids*, pages 1–23, Dordrecht, 2007. Springer Netherlands. ISBN 978-1-4020-5295-8.

P. Šmilauer and D. D. Vvedensky. Step-edge barriers on GaAs(001). *Phys. Rev. B*, 48:17603–17606, 1993.

R. Wang, M. Mujahid, Y. Duan, Z.-K. Wang, J. Xue, and Y. Yang. A review of perovskites solar cell stability. *Adv. Funct. Mater.*, 29(47):1808843, 2019.

W. Wang, J. Zhao, W. Wang, Z. Gai, N. Balke, M. Chi, H. N. Lee, W. Tian, L. Zhu, X. Cheng, D. J. Keavney, J. Yi, T. Z. Ward, P. C. Snijders, H. M. Christen, W. Wu, J. Shen, and X. Xu. Room-temperature multiferroic hexagonal $LuFeO_3$ films. *Phys. Rev. Lett.*, 110:237601, 2013.

T. Weckman, M. Shirazi, S. D. Elliott, and K. Laasonen. Kinetic Monte Carlo study of the atomic layer deposition of zinc oxide. *J. Phys. Chem. C*, 122(47): 27044–27058, 2018.

U. Zerweck, C. Loppacher, T. Otto, S. Grafström, and L. M. Eng. Accuracy and resolution limits of Kelvin probe force microscopy. *Phys. Rev. B*, 71:125424, 2005.

R.-Q. Zhang, X.-H. Xu, S.-Y. Zhang, and G. A. Gehring. Monte Carlo simulation of growth of binary bcc structured layers. *Phys. Rev. B*, 78:075419, 2008.

X. Zhang, H. Song, C. Tan, S. Yang, Y. Xue, J. Wang, and X. Zhong. Epitaxial growth and magnetic properties of h-$LuFeO_3$ thin films. *J. Mater. Sci.*, 52(24): 13879–13885, 2017.

Z. Zhou, R. Long, and O. V. Prezhdo. Why silicon doping accelerates electron polaron diffusion in hematite. *J. Am. Chem. Soc.*, 141(51):20222–20233, 2019.

Z. Zhu, X. J. Zheng, and W. Li. Multilayer growth of $BaTiO_3$ thin films via pulsed laser deposition: An energy-dependent kinetic Monte Carlo simulation. *Appl. Surf. Sci.*, 256(20):5876–5881, 2010.

List of publications

- R. Hrach, D. Novotný, V. Gabriel, S. Novák. Morphology of discontinuous metal films with pronounced secondary nucleation. *Vacuum*, 162, pp. 168–174, 2019

- V. Gabriel, P. Kocán, and V. Holý. Effective algorithm for simulations of layer-by-layer growth during pulsed-laser deposition. *Phys. Rev. E*, 102:063305, 2020.

- V. Gabriel, P. Kocán, S. Bauer, B. Nergis, A. Rodrigues, L. Horák, X. Jin, R. Schneider, T. Baumbach, and V. Holý. Effect of pulse laser frequency on PLD growth of $LuFeO_3$ explained by kinetic simulations of in-situ diffracted intensities. *Sci. Rep.*, 12(1):5647, 2022.

- V. Gabriel, P. Kocán, and V. Holý. Growth-rate model of epitaxial layer-by-layer growth by pulsed-laser deposition. *Phys. Rev. E*, 106:035302, 2022.

- J. Redondo, M. Reticcioli, V. Gabriel, D. Wrana, F. Ellinger, M. Riva, G. Franceschi, E. Rheinfrank, I. Sokolovic, Z. Jakub, F. Kraushofer, A. Alexander, L. L. Patera, J. Repp, M. Schmid, U. Diebold, G. S. Parkinson, C. Franchini, P. Kocán, and M. Setvín. Real-space investigation of polarons in hematite Fe_2O_3. *arXiv preprint arXiv:2303.17945*, 2023.